Object-Based Multipass InSAR via Robust Low-Rank Tensor Decomposition

Jian Kang, *Student Member, IEEE*, Yuanyuan Wang, *Member, IEEE*, Michael Schmitt, *Senior Member, IEEE*, and Xiao Xiang Zhu, *Senior Member, IEEE*

***Abstract*— The most unique advantage of multipass synthetic aperture radar interferometry (InSAR) is the retrieval of long-term geophysical parameters, e.g., linear deformation rates, over large areas. Recently, an object-based multipass InSAR framework has been proposed by Kang, as an alternative to the typical single-pixel methods, e.g., persistent scatterer interferometry (PSI), or pixel-cluster-based methods, e.g., SqueeSAR. This enables the exploitation of inherent properties of InSAR phase stacks on an object level. As a follow-on, this paper investigates the inherent low rank property of such phase tensors and proposes a Robust Multipass InSAR technique via Object-based low rank tensor decomposition. We demonstrate that the filtered InSAR phase stacks can improve the accuracy of geophysical parameters estimated via conventional multipass InSAR techniques, e.g., PSI, by a factor of 10–30 in typical settings. The proposed method is particularly effective against outliers, such as pixels with unmodeled phases. These merits, in turn, can effectively reduce the number of images required for a reliable estimation. The promising performance of the proposed method is demonstrated using high-resolution TerraSAR-X image stacks.**

***Index Terms*— Iterative reweight, low rank, object-based, synthetic aperture radar (SAR), SAR interferometry (InSAR), tensor decomposition.**

I. Introduction

A. Multipass InSAR

MULTIPASS or multibaseline synthetic aperture radar interferometry (InSAR) techniques, such as persistent scatterer interferometry (PSI) [2]–[11], distributed scatterer interferometry [12]–[17], and differential SAR tomography (D-TomoSAR) [18]–[23], are the most popular methods for the retrieval of geophysical parameters (namely, elevation and deformation parameters) for extended areas.

Past research on multipass InSAR was mainly focused on the optimal retrieval of the phase history parameters of individual scatterers, which can be considered in two categories: single-pixel-based methods and pixel-cluster-based methods. On the one hand, single-pixel-based methods, such as PSI [2]–[9] and D-TomoSAR [18]–[23], have been widely applied to the monitoring of urban areas. In particular, significant development has been made in D-TomoSAR, such as super-resolution D-TomoSAR methods based on compressive sensing [24]–[26] and combining D-TomoSAR with SAR geodesy [27], [28] to obtain absolute *Geodetic TomoSAR* [29] point clouds. On the other hand, pixel-cluster-based methods, such as SqueeSAR [12]–[14], [16], [30]–[32], CAESAR [33], and TomoSAR based on distributed scatterers [34]–[36], exploit statistical similarities between the neighboring pixels in order to retrieve the phase history parameters from their associated covariance matrices. Statistical ergodicity of the selected pixel clusters is always assumed in these methods for the estimation of the required sample covariance matrix. Likewise, nonlocal-InSAR (NL-InSAR) [37]–[40] also selects similar pixels but based on patch similarity.

Although some of the above-mentioned techniques do exploit information from multiple neighboring pixels or patches, no explicit semantic and geometric information that might be preserved in the images has been utilized. Zhu *et al.* [41] demonstrated that by introducing building footprints from OpenStreetMap as prior knowledge of pixels sharing similar heights into frameworks based on joint sparse reconstruction techniques, a highly accurate tomographic reconstruction can be achieved using only six interferograms instead of the typically required 20–100. Inspired by this, we recently proposed a general framework for object-based InSAR deformation reconstruction based on a tensor model with a regularization term, which is combined with semantic information shown in SAR images, i.e., classification labels of different objects like bridges, roofs, and façades, for an improvement of deformation retrieval [1], [42].

Based on the previous work, this paper seeks to investigate the inherent low-rank property of multipass InSAR phase tensors, given semantic prior knowledge of objects. We propose a novel robust tensor decomposition method using iterative reweighting to recover an outlier-free phase stack for the retrieval of the geophysical parameters.

B. Low-Rank Modeling

Low-rank modeling has been applied in many research fields of data analysis, since high-dimensional data are often embedded in a low-dimensional subspace [43]. One of the best

Manuscript received July 22, 2017; revised October 17, 2017; accepted December 19, 2017. Date of publication February 27, 2018; date of current version May 21, 2018. This work was supported in part by the China Scholarship Council, in part by the European Research Council (ERC) under the European Unions' Horizon 2020 Research and Innovation Program under Grant ERC-2016-StG-714087, and in part by the Helmholtz Association under the framework of the Young Investigators Group SiPEO under Grant VH-NG-1018. *(Corresponding author: Xiao Xiang Zhu.)*

J. Kang, Y. Wang, and M. Schmitt are with Signal Processing in Earth Observation, Technical University of Munich, 80333 Munich, Germany (e-mail: jian.kang@tum.de).

X. X. Zhu is with the Remote Sensing Technology Institute, German Aerospace Center (DLR), 82234 Wessling, Germany, and also with Signal Processing in Earth Observation, Technical University of Munich, 80333 Munich, Germany (e-mail: xiao.zhu@dlr.de).

Color versions of one or more of the figures in this paper are available online at http://ieeexplore.ieee.org.

Digital Object Identifier 10.1109/TGRS.2018.2790480

TABLE I
MATHEMATICAL NOTATIONS

$\mathcal{X}, \mathbf{X}, \mathbf{x}, x$	tensor, matrix, vector, scalar
$\mathbf{X}_{(n)}$	mode-n unfolding of tensor $\mathcal{X}$
$(R_1, R_2, \cdots, R_N)$	tensor multilinear rank, where $R_n = \mathrm{Rank}(\mathbf{X}_{(n)}), \quad n = 1, 2, \cdots, N$
$\langle \mathcal{X}, \mathcal{Y} \rangle$	inner product of tensor $\mathcal{X}$ and $\mathcal{Y}$, i.e. the sum of product of their entries
$\|\mathcal{X}\|_F$	Frobenius norm of tensor $\mathcal{X}$, i.e. $\|\mathcal{X}\|_F = \sqrt{\langle \mathcal{X}, \mathcal{X} \rangle}$
$\mathrm{vec}(\mathcal{X})$	vectorization of $\mathcal{X}$
$\|\mathcal{X}\|_1$	L_1 norm of tensor $\mathcal{X}$, i.e. $\|\mathcal{X}\|_1 = \|\mathrm{vec}(\mathcal{X})\|_1$
$\|\mathbf{X}\|_*$	matrix nuclear norm: the sum of its singular values, i.e. $\|\mathbf{X}\|_* := \sum_i \sigma_i$
$\mathcal{Y} = \mathcal{X} \times_n \mathbf{A}$	mode-n multiplication of tensor $\mathcal{X}$ and matrix $\mathbf{A}$, i.e. $\mathbf{Y}_{(n)} = \mathbf{A}\mathbf{X}_{(n)}$
$\otimes$	outer product
$\odot$	element-wise product

known low rank modeling approaches is principle component analysis (PCA) [44], which finds a low-rank version of the matrix by minimizing the approximation error to the original data matrix in a least-squares sense. It has been utilized for tackling various problems in remote sensing, such as SAR-image-based change detection [45], hyperspectral image denoising [46], data feature extraction [47], and so on. For applications in the InSAR field, PCA has recently been utilized for decomposing the scatterer covariance matrix in CAESAR [33] in order to separate layovered scatterers within individual pixels.

However, due to the assumption of independently and identically distributed Gaussian samples, PCA is sensitive to the existence of outliers. To robustly recover the low-rank data matrix, [48] proposed robust PCA (RPCA) to decompose the original matrix into a low-rank data matrix and a sparse outlier matrix. For instance, RPCA was deployed for hyperspectral image restoration in [49], and an RPCA-based approach for separating stationary and moving targets in SAR imaging was investigated in [50]. To deal with the data in a multidimensional case, [51] proposed a robust low-rank tensor recovery method called higher order RPCA (HoRPCA), which has been employed in our previous work [1] as an outlier filtering step for object-based InSAR deformation reconstruction.

C. Contributions of This Paper

To this end, the contributions of this paper are threefold.

1) Based on the tensor model of object-based InSAR phase stacks [1], we study their multidimensional low-rank property.
2) With this prior knowledge, we propose a novel InSAR phase tensor low-rank decomposition method using iterative reweighting, which is named Robust Multipass InSAR technique via Object-based low rank tensor decomposition (RoMIO).
3) Using simulation and real data, we demonstrate that the InSAR phase stacks filtered by RoMIO can improve the accuracy of geophysical parameters estimated via conventional multipass InSAR techniques, e.g., PSI, by a factor of 10–30 in typical settings, especially in the existence of outliers.

D. Structure of This Paper

The rest of this paper is organized as follows. Section II studies the low-rank property of such phase stacks. In Section III, the proposed RoMIO method is demonstrated for robustly recovering object-based InSAR phases. Experiments, including simulated and real InSAR data, are conducted to substantiate the performance of the proposed algorithm in Section IV. We discuss the experimental results in Section V. Section VI draws the conclusion of this paper.

II. LOW-RANK PROPERTY OF INSAR PHASE STACKS

A. Tensor Basics

A tensor can be considered as a multidimensional array. The *order* of a tensor is the number of its *modes* or *dimensions*. A tensor of order N in the complex domain can be denoted as $\mathcal{X} \in \mathbb{C}^{I_1 \times I_2 \ldots \times I_N}$ and its entries as $x_{i_1, i_2, \ldots, i_N}$. Specifically, vector $\mathbf{x}$ is a tensor of order one, and matrix $\mathbf{X}$ can be represented as a tensor of order two. *Fibers* are the higher order analogy of matrix rows and columns, which are defined by fixing every index but one. *Slices* of a tensor are obtained by fixing all but two indices. Matricization, also known as *unfolding*, is the process of reordering the elements of a tensor into a matrix. Specifically, the mode-n unfolding of tensor $\mathcal{X}$ is defined by $\mathbf{X}_{(n)}$ that is obtained by arranging the mode-n fibers as the columns of the matrix. The utilized tensor notations are summarized in Table I. The detailed introductions about multilinear algebra are presented in [52] and [53].

B. Tensor Model of Object-Based Multipass InSAR Phase Stacks

As proposed in our previous work [1], given object areas, such as façades and bridges or roofs, an InSAR phase stack can be represented by a 3-mode tensor: $\mathcal{G} \in \mathbb{C}^{I_1 \times I_2 \times I_3}$, where I_1 and I_2 represent the spatial dimensions in range and azimuth and I_3 denotes the number of SAR images. The phase tensor of the object can be modeled by

$$\overline{\mathcal{G}}(\mathbf{S}, \mathbf{P}) = \exp\left\{-j\left(\frac{4\pi}{\lambda r}\mathbf{S} \otimes \mathbf{b} + \frac{4\pi}{\lambda}\mathbf{P} \otimes \boldsymbol{\tau}\right)\right\} \tag{1}$$

where $\overline{\mathcal{G}}$ is the modeled phase tensor of the object, $\mathbf{b} \in \mathbb{R}^{I_3}$ is the vector of the spatial baselines, $\boldsymbol{\tau} \in \mathbb{R}^{I_3}$ is a warped time variable [21], e.g., $\boldsymbol{\tau} = \mathbf{t}$ for a linear motion, and $\boldsymbol{\tau} = \sin(2\pi(\mathbf{t} - t_0))$ for a seasonal motion model with temporal baseline $\mathbf{t}$ and time offset t_0. $\mathbf{S} \in \mathbb{R}^{I_1 \times I_2}$ and $\mathbf{P} \in \mathbb{R}^{I_1 \times I_2}$ are the unknown elevation and deformation maps to be estimated, respectively, λ is the wavelength of the radar signals,

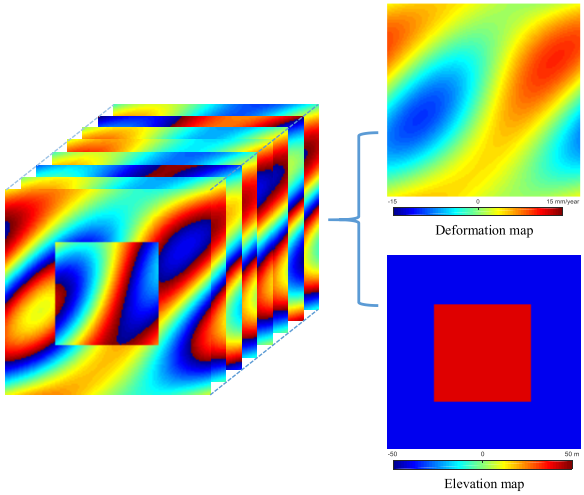

Fig. 1. One example of an object-based InSAR phase stack, which can be represented by the tensor model in (1). It shows the wrapped phase stack simulated by the synthetic linear deformation rates and elevations present on its right. The pattern of the simulated elevation map is comparable to that of urban objects in real scenarios. The simulated deformation map shows a more complex pattern, which represents continuously varying displacement in the scene. The elevation and deformation maps are designed to be spatially uncorrelated.

and r denotes the range between radar and the observed object. The symbol $\otimes$ denotes the outer product [53]. A simulated example of such a phase stack is shown in Fig. 1. It shows the wrapped phase stack, and the simulated linear deformation rates and elevations from which the phase stack is constructed. The pattern of the simulated elevation map is comparable to that of urban objects in real scenarios. The simulated deformation map shows a more complex pattern, which represents continuously varying displacement in the scene. The elevation and deformation maps are designed to be spatially uncorrelated.

Such phase tensors in urban areas usually experience an inherent low-rank nature, since it can be generally assumed that $\mathbf{S}$ and $\mathbf{P}$ follow certain regular structure or homogeneous pattern because of the regular man-made structures in urban areas. Moreover, the observed SAR images of urban object areas are usually highly correlated along the temporal dimension. Such a low-rank property will be demonstrated and investigated in the following chapter.

C. Low-Rank Study of InSAR Phase Stacks

Since PCA is the most basic low-rank decomposition method for matrices, it will be employed in this section to demonstrate the low-rank property of an InSAR phase tensor. PCA is usually realized by singular value decomposition (SVD) [54]. Given a matrix $\mathbf{X} \in \mathbb{C}^{I_1 \times I_2}$ and its SVD, i.e., $\mathbf{USV}^H$, the rank R approximation of $\mathbf{X}$ by truncating $\mathbf{S}$ up to R dominant singular values is the matrix $\mathbf{X}_R = \mathbf{U}_R\mathbf{S}_R\mathbf{V}_R^H$, where the $R \times R$ diagonal matrix $\mathbf{S}_R$ satisfies $\mathbf{S}_R(i,i) = \mathbf{S}(i,i), i = 1, 2, \ldots, R$, $\mathbf{U}_R$ is composed by the first R columns of $\mathbf{U}$, and $\mathbf{V}_R^H$ consists of the first R rows of $\mathbf{V}^H$. This is also known as truncated SVD.

As a higher dimensional extension of SVD, higher order SVD (HoSVD), also known as Tucker decomposition [55], can provide a tensor data compression based on the low-rank approximation, as shown in Fig. 2. It decomposes a tensor into a core tensor multiplied by a matrix along each mode. Specifically, for a 3-mode tensor, $\mathcal{X}^{I_1 \times I_2 \times I_3}$, we have

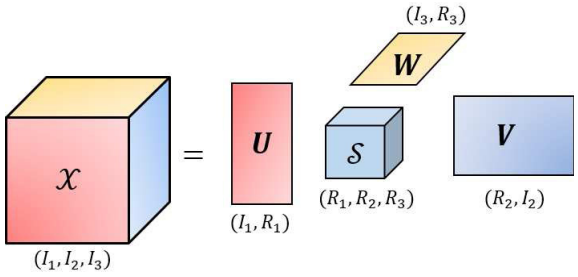

Fig. 2. Illustration of HoSVD of a 3-mode tensor [53].

$$\mathcal{X} = \mathcal{S} \times_1 \mathbf{U} \times_2 \mathbf{V} \times_3 \mathbf{W} \tag{2}$$

where $\mathbf{U}^{I_1 \times R_1}$, $\mathbf{V}^{I_2 \times R_2}$, and $\mathbf{W}^{I_3 \times R_3}$ are the factor matrices that can be considered as the principal components in each mode [52], $\mathcal{S}^{R_1 \times R_2 \times R_3}$ is the so-called *core tensor*, and symbol $\times_n$ is mode-n multiplication between tensor and matrix [53]. (R_1, R_2, R_3) is the so-called *multilinear rank* of $\mathcal{X}$. They fulfill the inequalities $R_1 \leqslant \min(I_1, I_2 I_3)$, $R_2 \leqslant \min(I_2, I_1 I_3)$, and $R_3 \leqslant \min(I_3, I_1 I_2)$.

A low-rank approximation of $\mathcal{X}$ can be realized by the truncated HoSVD. Taking $\mathcal{X}^{I_1 \times I_2 \times I_3}$ as an example, we can define its tensor approximation with multilinear rank (K_1, K_2, K_3), where $K_1 \leqslant R_1$, $K_2 \leqslant R_2$, and $K_3 \leqslant R_3$, by the following truncated HoSVD:

$$\mathcal{X}^{I_1 \times I_2 \times I_3} \approx \mathcal{S}^{K_1 \times K_2 \times K_3} \times_1 \mathbf{U}^{I_1 \times K_1} \times_2 \mathbf{V}^{I_2 \times K_2} \times_3 \mathbf{W}^{I_3 \times K_3} \tag{3}$$

where $\mathbf{U}^{I_1 \times K_1}$, $\mathbf{V}^{I_2 \times K_2}$, and $\mathbf{W}^{I_3 \times K_3}$ are created by storing the first $K_i (i = 1, 2, 3)$ singular vectors of $\mathbf{U}$, $\mathbf{V}$, and $\mathbf{W}$ and replacing the left $R_i - K_i (i = 1, 2, 3)$ vectors by zeros, and $\mathcal{S}^{K_1 \times K_2 \times K_3}$ is created in a similar way. Such truncated HoSVD finds a low-rank tensor approximation of the original tensor $\mathcal{X}$ in a least-squares sense.

In order to investigate the low-rank property of an InSAR phase tensor, the normalized singular values $(\sigma_i / \max(\sigma_i))$ of the mode-1, -2 and -3 unfolding matrices of a simulated noise-free complex-valued phase tensor $\overline{\mathcal{G}} \in \mathbb{C}^{100 \times 100 \times 50}$ (shown in Fig. 1) are shown in Fig. 3. It can be observed that the singular values of the three unfolding matrices decay rapidly, which indicates the low-rank nature of the original tensor. The low-rank tensor approximation $\tilde{\mathcal{G}}$ of $\overline{\mathcal{G}}$ can be obtained by the truncated HoSVD with a predefined threshold. As shown in Fig. 4, we calculate the mean-square-error (MSE) values of the real-valued residual phases between the approximated tensor $\tilde{\mathcal{G}}$ and the original tensor $\overline{\mathcal{G}}$, i.e., $\mathrm{MSE}(\mathrm{angle}(\tilde{\mathcal{G}} \odot \mathrm{conj}(\overline{\mathcal{G}})))$, with respect to different thresholds, where $\odot$ denotes the elementwise product and $\mathrm{conj}(\cdot)$ is the complex conjugate operator. According to the plot, the original InSAR phase stack can be well approximated by the low-rank tensor $\tilde{\mathcal{G}}$ with acceptable errors. For example, at the thresholding value of 0.21, the MSE value of the real-valued residual phases

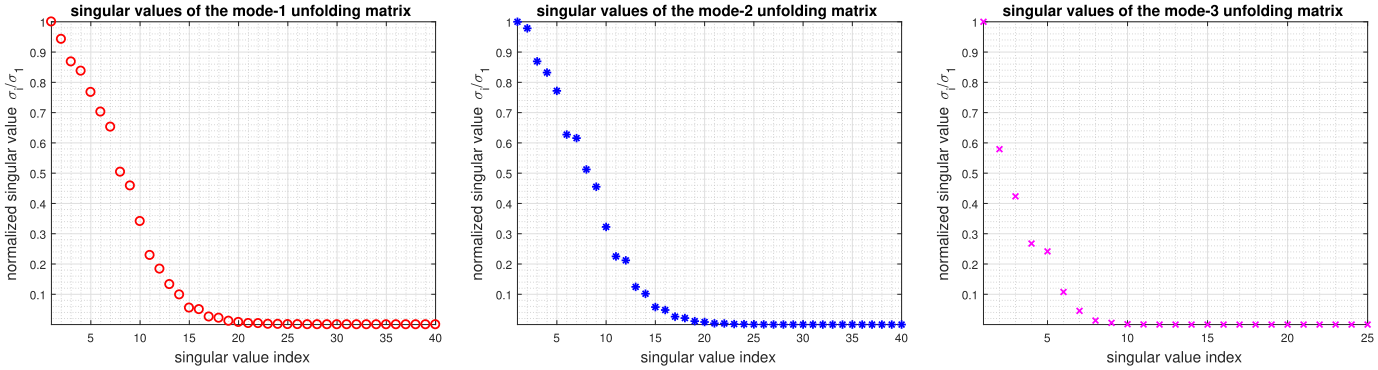

Fig. 3. Normalized singular values of mode-1, -2, and -3 unfolding matrices of the simulated example of the complex-valued InSAR phase stack shown in Fig. 1. For visualization, we just plot the first 40 out of all the 128 normalized singular values of mode-1 and -2 unfolding matrices. It is demonstrated that the singular values of the three unfolding matrices decay rapidly, which indicates the low-rank structure of the original tensor.

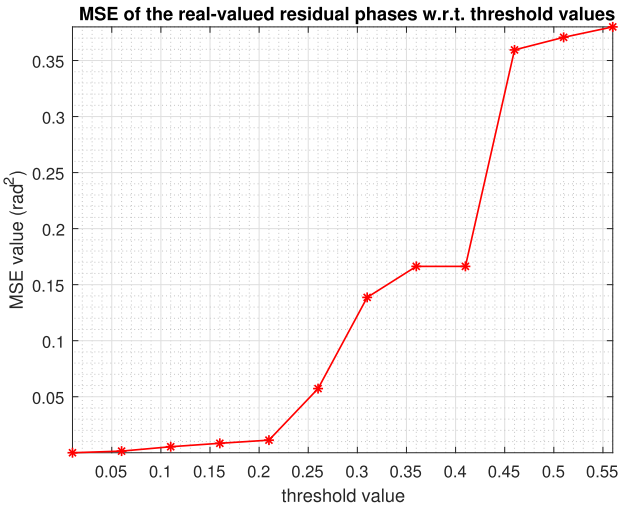

Fig. 4. MSE values of the real-valued residual phases between the low-rank approximated tensor $\tilde{\mathcal{G}}$ and the original tensor $\overline{\mathcal{G}}$, i.e., MSE(angle($\tilde{\mathcal{G}} \odot \text{conj}(\overline{\mathcal{G}})$)) with respect to different threshold values.

between $\tilde{\mathcal{G}}$ [its multilinear rank is $(11, 12, 5)$] and $\overline{\mathcal{G}}$ is around $0.01[\text{rad}^2]$, which is equivalent to an uncertainty of 0.2 [mm/year] in linear deformation rate or 0.69 [m] in elevation at the baseline configuration of the simulated data. Such a low-rank property is often embedded in images. This is especially true in urban areas, where man-made objects with regular shapes are abundant.

Such a low-rank property also exists in real data, which usually contains full rank noise. To this end, the normalized singular values of an experimental TerraSAR-X phase tensor with a roof area (see Fig. 5) are shown in Fig. 6. The associated phase tensor has the dimensions of $256 \times 320 \times 29$. It can be seen that the normalized singular values decay rapidly and most of them are below 0.2, which indicates the low-rank structure of the InSAR phase tensor.

III. Robust Phase Recovery via Iteratively Reweighted Tensor Decomposition

For the case of real data, outliers, e.g., unmodeled phases, usually exist in the observed phase stack. To tackle this challenge, we propose a novel robust tensor decomposition method—robust iteratively reweighted tensor decomposition.

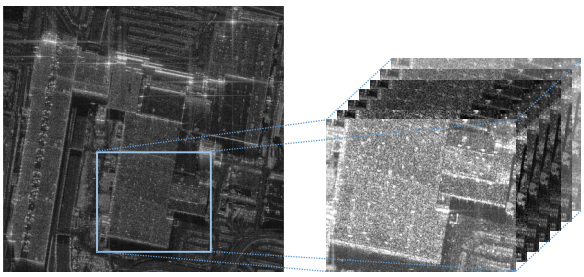

Fig. 5. InSAR phase tensor example of TerraSAR-X data with a roof area (blue rectangle) of the Las Vegas Convention Center. For the illustration, we show the amplitudes of the multipass SAR images.

A. Robust Low-Rank Tensor Decomposition

Different from HoSVD where the approximation error is minimized in a least-squares sense, robust low-rank tensor decomposition minimizes the rank with L_0 norm of the approximation error

$$\{\hat{\mathcal{X}}, \hat{\mathcal{E}}\} = \underset{\mathcal{X},\mathcal{E}}{\text{argmin}}\, \text{rank}(\mathcal{X}) + \gamma \|\mathcal{E}\|_0, \quad \text{s.t. } \mathcal{X} + \mathcal{E} = \mathcal{G} \quad (4)$$

where $\mathcal{G}$ is the observed InSAR phase tensor, $\mathcal{E}$ models the tensor of sparse outliers, $\hat{\mathcal{X}}$ and $\hat{\mathcal{E}}$ are the recovered outlier-free phase tensor and the estimated outlier tensor, respectively, $\text{rank}(\mathcal{X})$ refers to the multilinear rank of $\mathcal{X}$, $\|\mathcal{E}\|_0$ denotes the L_0 norm of $\mathcal{E}$, i.e., $\|\mathcal{E}\|_0 = \|\text{vec}(\mathcal{E})\|_0$, and γ is the regularization parameter.

This problem is NP-hard due to the minimization of the multilinear rank and the L_0 norm. Regarding this, [51] suggested to replace (4) by the following convex optimization problem:

$$\{\hat{\mathcal{X}}, \hat{\mathcal{E}}\} = \underset{\mathcal{X},\mathcal{E}}{\text{argmin}}\, \|\mathcal{X}\|_* + \gamma \|\mathcal{E}\|_1, \quad \text{s.t. } \mathcal{X} + \mathcal{E} = \mathcal{G}. \quad (5)$$

It relaxes the tensor multilinear rank to the tensor nuclear norm $\|\mathcal{X}\|_*$, which is the sum of the N nuclear norm $\sum_n \|\mathbf{X}_{(n)}\|_*$ of the mode-n unfoldings of $\mathcal{X}$, i.e., $\|\mathcal{X}\|_* = \sum_n \|\mathbf{X}_{(n)}\|_*$, and by replacing the tensor L_0 norm with the convex L_1 norm, i.e., $\|\mathcal{E}\|_1 = \|\text{vec}(\mathcal{E})\|_1$. This is known as HoRPCA, which is a tensor extension of the matrix RPCA [48].

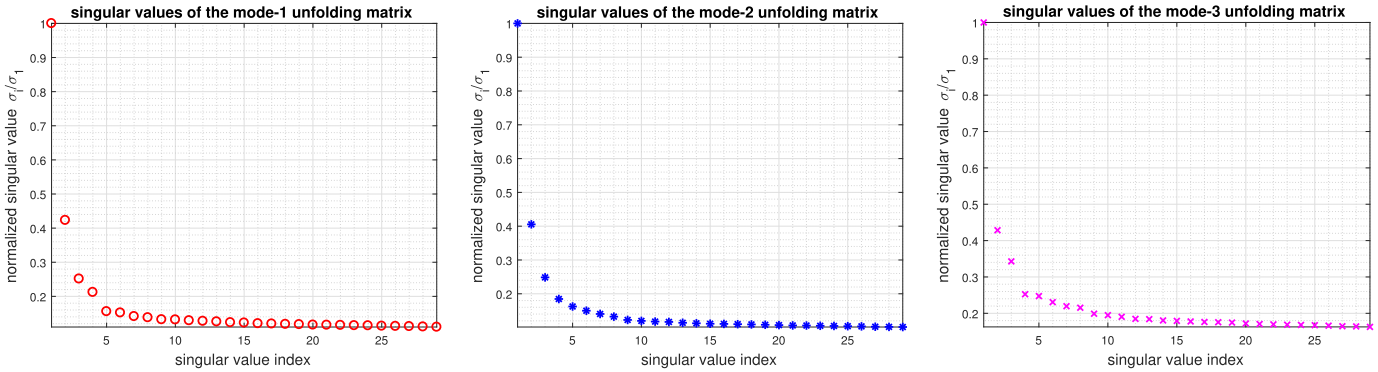

Fig. 6. Normalized singular values of mode-1, -2 and -3 unfolding matrices of the complex-valued InSAR phase stack shown in Fig. 5. For visualization, we just plot the first 29 normalized singular values of mode-1 and -2 unfolding matrices. It is demonstrated that the normalized singular values of the three unfolding matrices decay rapidly, and most of them are below 0.2, which indicates low-rank structures of InSAR phase tensors in real cases.

B. Robust Iteratively Reweighted Tensor Decomposition

In order to better approximate the rank of a matrix and the L_0 norm of a vector, [56] and [57] proposed a reweighted nuclear norm and an L_1 minimization scheme by enhancing the low rank and sparsity simultaneously during the optimization. The reweighted L_1 norm is defined as $\|\mathbf{w}\odot\mathbf{x}\|_1$, where $\mathbf{w}$ is the weight vector that updates adaptively for enhancing the sparsity of $\mathbf{x}$. It is worth noting that if each element of $\mathbf{w}$ is exactly the inverse absolute value of the corresponding element of $\mathbf{x}$, i.e., $w_i = (1/|x_i|)$, the reweighted L_1 norm equals the L_0 norm of $\mathbf{x}$, i.e., $\|(1/|\mathbf{x}|)\odot\mathbf{x}\|_1 = \|\mathbf{x}\|_0$. For the low-rank enhancement, the nuclear norm for matrix X is replaced by a reweighted version $\|\mathbf{w}\odot\boldsymbol{\sigma}(\mathbf{X})\|_1$. Likewise, if we have $w_i = (1/(\sigma_i(\mathbf{X})))$, then the reweighted nuclear norm turns into the rank of the matrix $\mathbf{X}$, i.e., $\|\mathbf{w}\odot\boldsymbol{\sigma}(\mathbf{X})\|_1 = \text{rank}(\mathbf{X})$.

Inspired by this, we extend the reweighting scheme to the tensor case. By introducing the weights for enhancing the low rank of $\mathcal{X}$ and the sparsity $\mathcal{E}$, the optimization problem is

$$\{\hat{\mathcal{X}},\hat{\mathcal{E}}\} = \underset{\mathcal{X},\mathcal{E}}{\text{argmin}} \sum_{n=1}^{N} \|\mathbf{w}_{\mathcal{L},n}\odot\boldsymbol{\sigma}(\mathbf{X}_{(n)})\|_1 + \gamma\,\|\mathcal{W}_{\mathcal{E}}\odot\mathcal{E}\|_1 \quad \text{s.t. } \mathcal{X}+\mathcal{E}=\mathcal{G} \tag{6}$$

where $\mathbf{w}_{\mathcal{L},n}$ is the weight vector for the singular values of the mode-n unfolding matrix $\mathbf{X}_{(n)}$ of $\mathcal{X}$ and $\mathcal{W}_{\mathcal{E}}$ is the weight tensor for $\mathcal{E}$. Note that if all weights are set to 1, (6) will be equivalent to (5).

C. Optimization by Alternating Direction Method of Multipliers

The optimization problem (6) can be solved by the alternating direction method of multiplier (ADMM) framework [58]. The constraint optimization problem in (6) is first converted to its augmented Lagrangian function, yielding

$$L_\mu(\mathcal{X},\mathcal{E},\mathcal{Y}) = \sum_{n=1}^{N} \|\mathbf{w}_{\mathcal{L},n}\odot\boldsymbol{\sigma}(\mathbf{X}_{(n)})\|_1 + \gamma\,\|\mathcal{W}_{\mathcal{E}}\odot\mathcal{E}\|_1 - \langle\mathcal{Y},\mathcal{X}+\mathcal{E}-\mathcal{G}\rangle + \frac{1}{2\mu}\|\mathcal{X}+\mathcal{E}-\mathcal{G}\|_F^2 \tag{7}$$

where $\mathcal{Y}$ denotes the introduced dual-variable and μ is the penalty parameter. The ADMM takes advantage of splitting one difficult optimization problem into several subproblems, where each of them has a closed-form solution. Accordingly, the minimization of L_μ with respect to each variable can be solved by optimizing the following subproblems.

1) $\mathcal{X}$ Subproblem: By fixing $\mathcal{E}$ and $\mathcal{Y}$, the subproblem of L_μ with respect to $\mathcal{X}$ can be rewritten as

$$\min_{\mathcal{X}} \sum_{n=1}^{N} \|\mathbf{w}_{\mathcal{L},n}\odot\boldsymbol{\sigma}(\mathbf{X}_{(n)})\|_1 + \frac{1}{2\mu}\|\mathcal{X}+\mathcal{E}-\mathcal{G}-\mu\mathcal{Y}\|_F^2. \tag{8}$$

This subproblem can be solved by the nonuniform singular value thresholding (NSVT) operator [57], [59]. Taking matrix $\mathbf{A}$ as an example, given the thresholding weight vector $\mathbf{w}$, NSVT is defined as $\mathcal{T}_{\mathbf{w}}(\mathbf{A}) := \mathbf{U}\text{diag}(\max(\sigma_i - w_i, 0))\mathbf{V}$ with $\mathbf{U}$, $\mathbf{V}$, and σ_i calculated by SVD of $\mathbf{A}$.

2) $\mathcal{E}$ Subproblem: By fixing $\mathcal{X}$ and $\mathcal{Y}$, the subproblem of L_μ with respect to $\mathcal{E}$ has the following form:

$$\min_{\mathcal{E}} \gamma\,\|\mathcal{W}_{\mathcal{E}}\odot\mathcal{E}\|_1 + \frac{1}{2\mu}\|\mathcal{X}+\mathcal{E}-\mathcal{G}-\mu\mathcal{Y}\|_F^2. \tag{9}$$

This weighted L_1-norm optimization subproblem can be solved by the nonuniform soft thresholding operator, which is defined as $\mathcal{S}_{\mathcal{W}}(\mathcal{A}) := \text{sign}(\mathcal{A})\odot\max(|\mathcal{A}|-\mathcal{W},0)$, with $|\mathcal{A}| = \text{sign}(\mathcal{A})\odot\mathcal{A}$.

3) $\mathcal{Y}$ Updating: The dual-variable $\mathcal{Y}$ can be updated by

$$\mathcal{Y} = \mathcal{Y} - \frac{1}{\mu}(\mathcal{X}+\mathcal{E}-\mathcal{G}). \tag{10}$$

4) Weight Updating: The weight vector $\mathbf{w}_{\mathcal{L},n}, n=1,\ldots,N$ and the weight tensor $\mathcal{W}_{\mathcal{E}}$ can be updated by

$$\mathbf{w}_{\mathcal{L},n} = \frac{1}{\boldsymbol{\sigma}(\mathbf{X}_{(n)})+\epsilon_{\mathcal{L}}}, \quad \mathcal{W}_{\mathcal{E}} = \frac{1}{|\mathcal{E}|+\epsilon_{\mathcal{E}}} \tag{11}$$

where $\epsilon_{\mathcal{L}}$ and $\epsilon_{\mathcal{E}}$ are the predetermined positive constants.

The detailed ADMM pseudocode for solving (6) is summarized in Algorithm 1.

Using a predefined convergence condition, the solutions ($\hat{\mathcal{X}}$ and $\hat{\mathcal{E}}$) can be obtained, i.e., the outlier-free InSAR phase tensor and the sparse outlier tensor, respectively. To this end, by applying conventional multipass InSAR techniques,

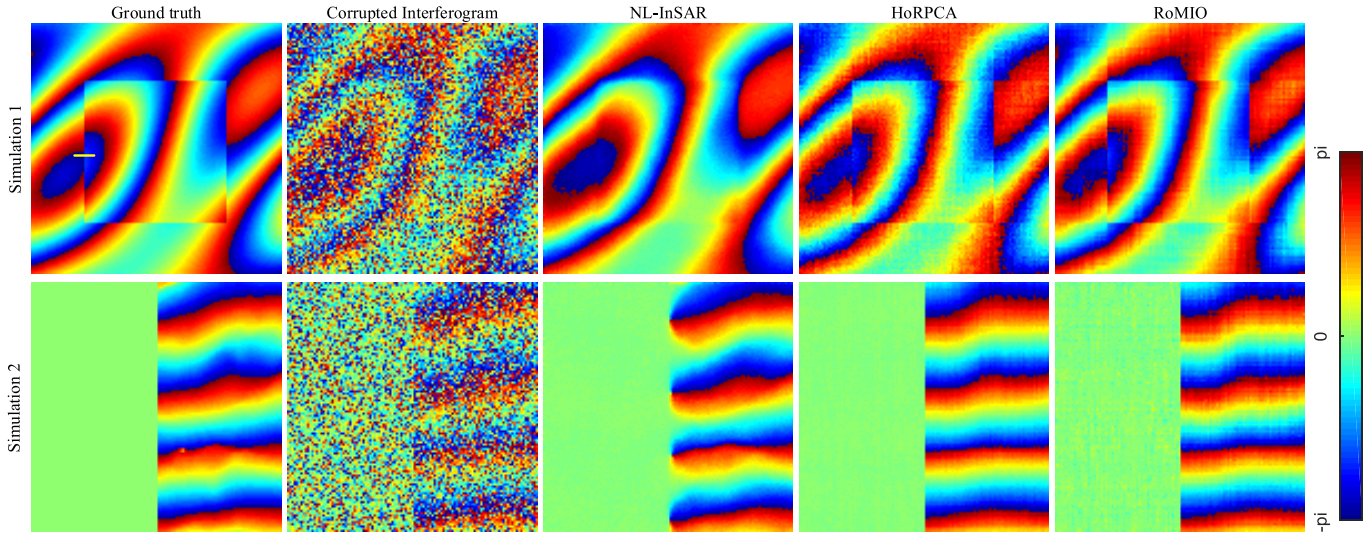

Fig. 7. Plots of one interferogram in the two simulated InSAR phase stacks, generated by the corresponding geophysical parameters shown in Fig. 9, the corrupted phases with an SNR of 5 dB and 30% outliers, and the recovered results by three methods. Although the NL-InSAR result can maintain the smooth fringes very well, the edges of rectangle in the middle are more blurred compared with the other two results. This can be clearly observed at the two cropped parts in Fig. 8. Compared with HoRPCA, the proposed method can better keep the original structure of the interferogram, since it can better capture the low-rank structure of the data and model the sparse outliers by enhancing the low rank and the sparsity.

e.g., PSI [2], on $\hat{\mathcal{X}}$, we can robustly retrieve the geophysical parameters.

Algorithm 1 RoMIO Solved by ADMM

Input: $\mathcal{G}, \gamma, \mu, N, \epsilon_{\mathcal{L}} = \epsilon_{\mathcal{E}} = 1 \times 10^{-3}$

Initialize $\mathcal{X}^{(0)} = \mathcal{E}^{(0)} = \mathcal{Y}^{(0)} = 0$

for $k = 0$ to $k_{\max}$ **do**

NSVT on the mode-n, $n = 1, \ldots, N$ unfolding of $\mathcal{G} + \mu\mathcal{Y}^{(k)} - \mathcal{E}^{(k)}$,

then, folding mode-n tensors and averaging them by N

$$\mathcal{X}^{(k+1)} \leftarrow \frac{1}{N}\sum_{n=1}^{N} \mathcal{T}_{n,\mu N \mathbf{w}_{\mathcal{L},n}^{(k)}}(\mathbf{G}_{(n)} + \mu \mathbf{Y}_{(n)}^{(k)} - \mathbf{E}_{(n)}^{(k)}),$$

where $\mathcal{T}_{n,\mu N \mathbf{w}_{\mathcal{L},n}^{(k)}}(\cdot) := \text{fold}_n(\mathcal{T}_{\mu N \mathbf{w}_{\mathcal{L},n}^{(k)}}(\cdot))$,

NST on the the tensor $\mathcal{G} + \mu\mathcal{Y}^{(k)} - \mathcal{X}^{(k+1)}$:

$$\mathcal{E}^{(k+1)} \leftarrow \mathcal{S}_{\mu\gamma \mathcal{W}_{\mathcal{E}}^{(k)}}(\mathcal{G} + \mu\mathcal{Y}^{(k)} - \mathcal{X}^{(k+1)}),$$

$$\mathcal{Y}^{(k+1)} \leftarrow \mathcal{Y}^{(k)} - \frac{1}{\mu}(\mathcal{X}^{(k+1)} + \mathcal{E}^{(k+1)} - \mathcal{G}),$$

Updating weights:

$$\mathbf{w}_{\mathcal{L},n}^{(k+1)} = \frac{1}{\boldsymbol{\sigma}(\mathbf{X}_{(n)}^{(k+1)}) + \epsilon_{\mathcal{L}}}, \quad \mathcal{W}_{\mathcal{E}}^{(k+1)} = \frac{1}{|\mathcal{E}^{(k+1)}| + \epsilon_{\mathcal{E}}},$$

if convergence **then**

break

end if

end for

Output: $(\hat{\mathcal{X}}, \hat{\mathcal{E}})$

IV. Experimental Results

A. Simulations

We simulated two multipass InSAR phase stacks of 128 × 128 pixels by 25 images with different spatial patterns. The corresponding linear deformation and elevation maps are shown in Fig. 9. Note that the two geophysical maps of Simulation 1 are spatially uncorrelated, while those of Simulation 2 are highly correlated. Their linear deformation rates range from −15 [mm/year] to 15 [mm/year] and elevation values are from −50 [m] to 50 [m]. The spatial baseline and the temporal baseline were chosen to be comparable to those of TerraSAR-X. Uncorrelated complex circular Gaussian noise was added to the two simulated stacks with an SNR of 5 dB, i.e., according to the persistent scatterer model. To simulate sparse outliers in the stacks, 30% of pixels randomly selected from the phase tensor were replaced with uniformly distributed phases.

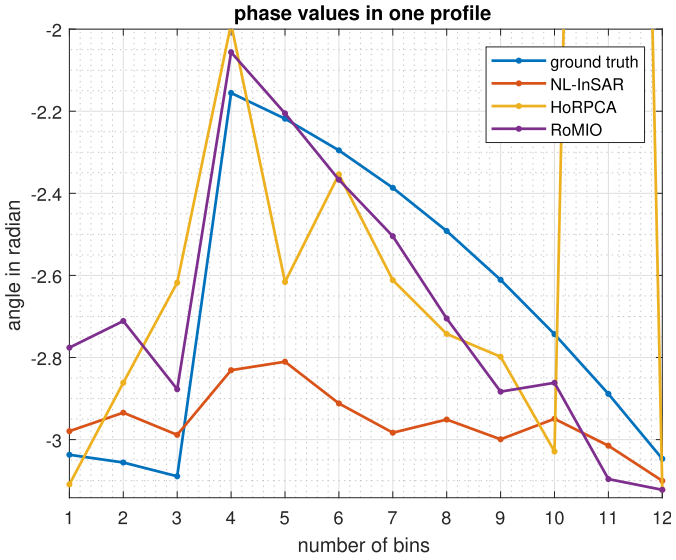

Fig. 8. Profiles of the estimated phases marked by the short yellow line segment in Fig. 7. It is obvious to show that the estimations of this area are blurred in the NL-InSAR result compared with the others.

TABLE II
MSE PERFORMANCES OF NL-INSAR, HORPCA, AND ROMIO ON THE SIMULATIONS SHOWN IN FIG. 7

		Simulation 1			Simulation 2		
		NL-InSAR	HoRPCA	RoMIO	NL-InSAR	HoRPCA	RoMIO
Mean Square Error (MSE) [rad^2]	30% outliers	**0.03**	0.04	**0.03**	**0.03**	0.04	0.04
	40% outliers	0.05	0.07	**0.04**	**0.05**	0.06	**0.05**
	50% outliers	0.12	0.12	**0.06**	0.07	0.12	**0.06**

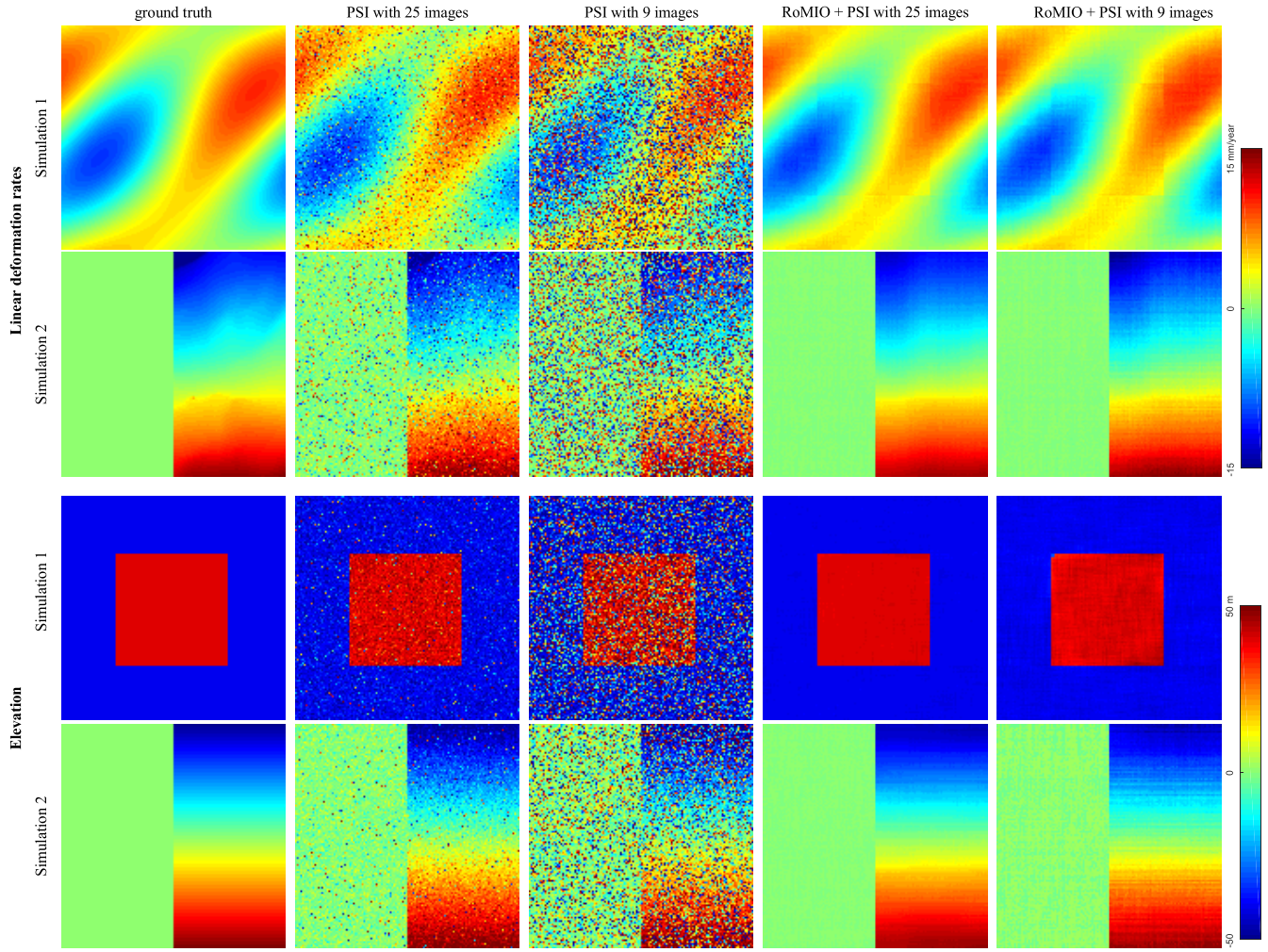

Fig. 9. Simulated ground truth linear deformation rates and elevations of the two simulations along with the estimated results by PSI and RoMIO + PSI with 25 and 9 SAR images. The results of PSI contain outliers. This is especially true for the result from a subset of the stack. The reason is that the periodogram method in PSI is only asymptotically optimal, which means large bias is very likely to occur at a low number of images. In contrast, the proposed method can robustly recover the parameters both using the full stack and a subset of the stack. That is to say the proposed method can, in turn, effectively reduce the number of images required for a reliable estimation.

For visualizing the performance of the proposed method, we chose one interferogram from the recovered phase tensor $\hat{\mathcal{X}}$ and visually compared it with those obtained by NL-InSAR [37] and HoRPCA [1] in Fig. 7. Since NL-InSAR is designed for denoising one interferogram, whereas the others make use of the full image stack, to achieve a relatively fair comparison, the NL-InSAR result was obtained by averaging the results from 25 simulations of InSAR phase stacks. In our method, the spatial size of the tensor is set as 128×128 (i.e., the whole stack as one tensor), γ is set to be 4.4×10^{-4}, and μ is kept constant at the value $10 \times \text{std}(\text{vec}(\mathcal{G}))$. The experiments for the associated parameter setting will be introduced in Section V-B. The search window size and the patch size in NL-InSAR are 21×21 and 5×5, respectively. In addition, the phase profile marked by the short yellow line segment in Fig. 7 is shown in Fig. 8. For a quantitative evaluation, we list the MSE values of the real-valued residual phases between the recovered phase tensor and the ground truth, i.e., MSE(angle($\hat{\mathcal{X}} \odot \text{conj}(\mathcal{X})$)), in the cases of 30%, 40%, and 50% of outliers in Table II.

Furthermore, we compared the estimated results of geophysical parameters by PSI and the proposed RoMIO + PSI,

TABLE III
QUANTITATIVE STUDY OF THE RESULTS IN FIG. 9

		Deformation [mm/year]		Elevation [m]	
		SD	bias	SD	bias
simulation 1	PSI (25 images)	2.68	−0.01	8.18	0.42
	PSI (9 images)	7.41	−0.04	31.56	7.02
	RoMIO+PSI (25 images)	0.27	0.01	0.39	−0.05
	RoMIO+PSI (9 images)	0.29	−0.02	1.59	0.01
simulation 2	PSI (25 images)	2.76	0.02	7.27	0.07
	PSI (9 images)	9.16	0.05	21.12	0.21
	RoMIO+PSI (25 images)	0.31	0.01	0.98	0.02
	RoMIO+PSI (9 images)	0.31	−0.01	1.17	0.13

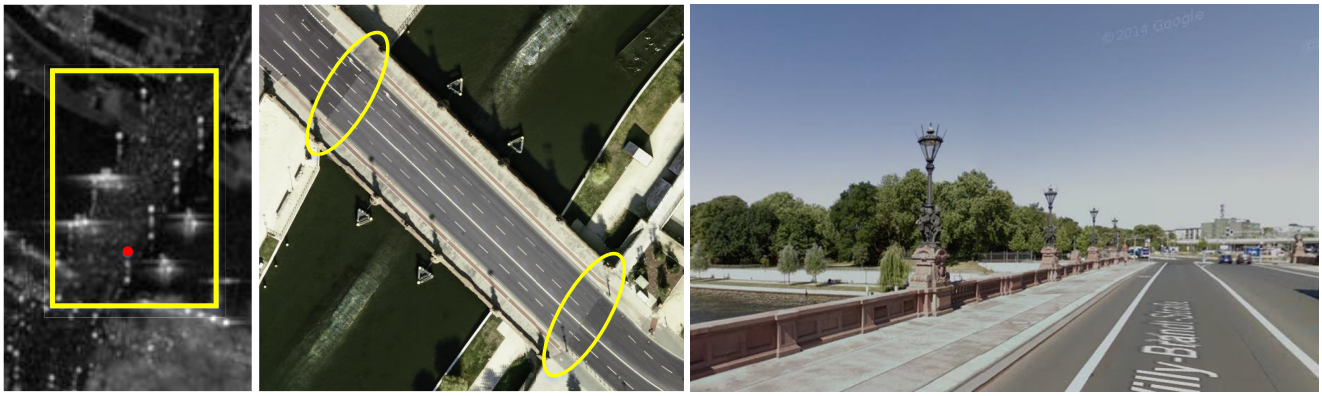

Fig. 10. (Left) TerraSAR-X test image of one bridge area in Berlin as cropped by the yellow rectangle. Red point: reference point for the elevation and seasonal motion reconstruction in this area. (Middle) Associated orthorectified optical image generated using semiglobal matching [61]. (Right) Streetview image from Google StreetView.

using the simulated data. The outlier percentage was set to 30% and SNR was 5 dB. α was set to 5×10^{-3}. The results are shown in Fig. 9. The first two rows are the estimates of linear deformation rates of the two simulations and the last two rows are the corresponding elevation estimates. In addition to the experiments based on the full stack of 25 SAR images, experiments using only nine images were conducted in order to test the RoMIO's capability to handle small stacks. For the associated quantitative evaluation, we calculated both bias and standard deviation (SD) of the results and presented them in Table III. To study the minimum number of images for RoMIO to achieve a reliable estimation, we plot the SD of the deformation estimates obtained by RoMIO + PSI with respect to a decreasing number of SAR images down to 7.

B. Real Data

1) Berlin Bridge: The first TerraSAR-X test area is a bridge in Berlin, Germany, which is marked by the yellow rectangle shown in Fig. 10 (left), where the reference point for the elevation and seasonal motion reconstruction is plotted in red. Fig. 10 (middle) shows the corresponding orthorectified optical image [61] and Fig. 10 (right) shows a streetview image from Google StreetView are also displayed. The InSAR stack contains over 100 images. However, in order to test the performance under a low number of images, 20 and 9 SAR images were selected from the full stack, respectively. They were selected to be similar in their distributions and spans of the temporal and spatial baselines, so that the Cramér–Rao bounds of the estimates are comparable. The baselines were also chosen to be close to uniform distribution. The 2-D baseline distribution of the selected images can be seen in Fig. 11. The estimated amplitudes of the seasonal motion and the elevation by PSI and RoMIO + PSI are shown in Fig. 12.

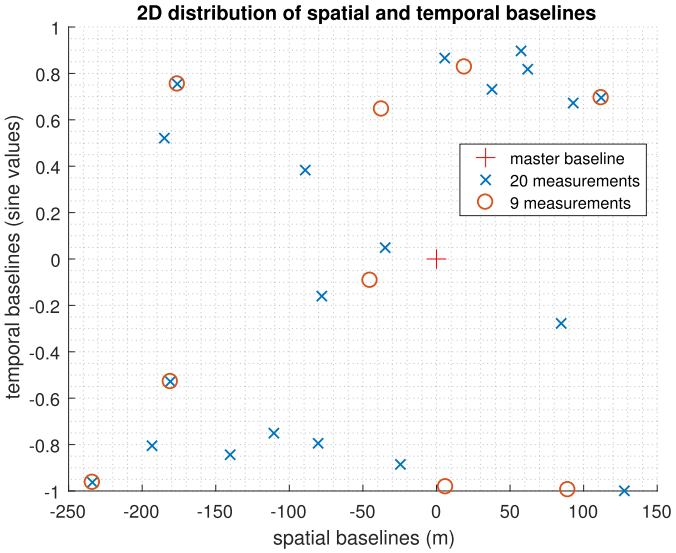

Fig. 11. 2-D distribution of spatial and temporal baselines of the selected 20 and 9 measurements for reconstruction. The baselines were also chosen to be close to uniform distribution.

2) Las Vegas Convention Center: Another TerraSAR-X test data set is the Las Vegas Convention Center, Las Vegas, NV, USA, as shown in Fig. 13. The total number of SAR images is 29. Since the building structure is complex and its spatial area is relatively large (800×850 pixels), we separately

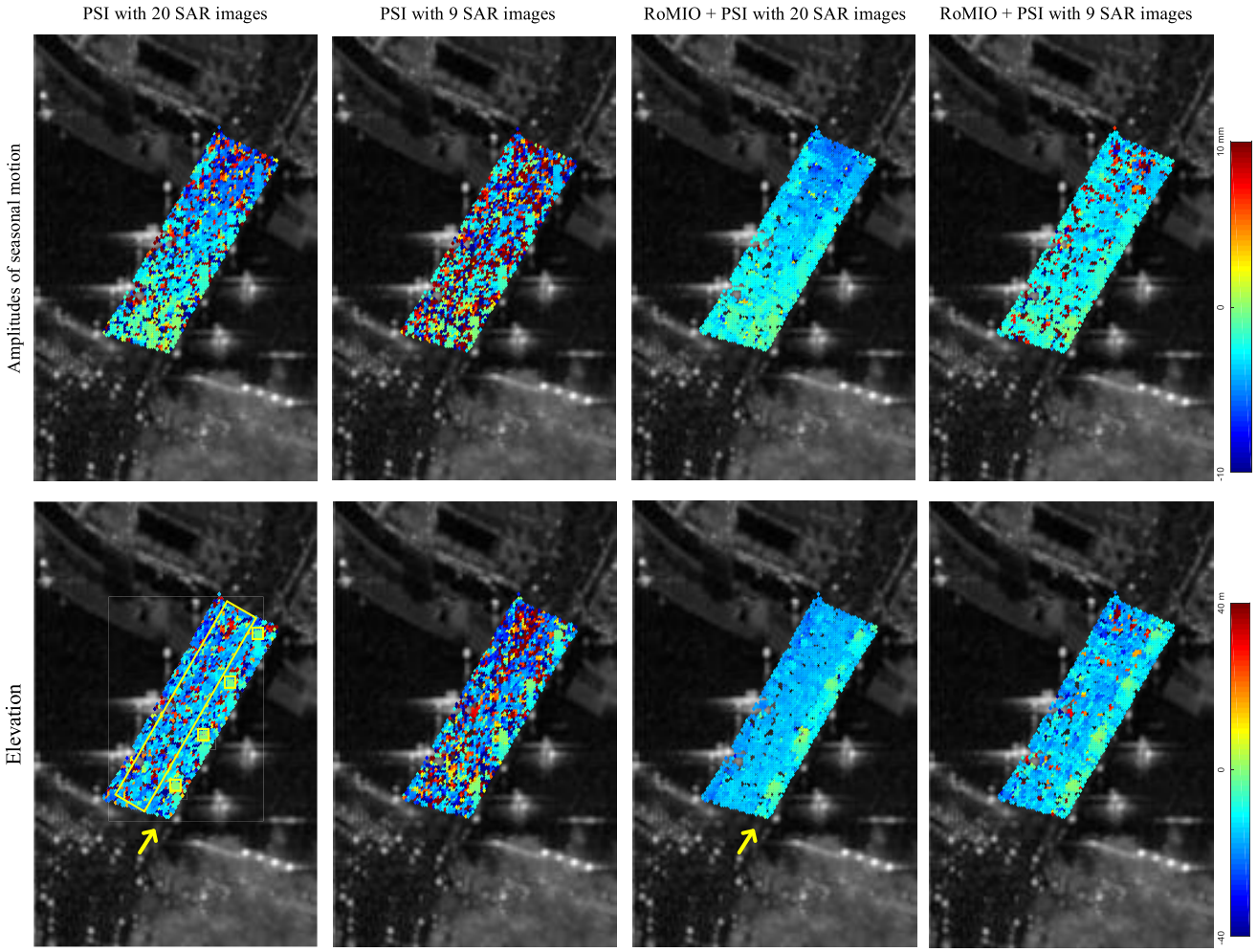

Fig. 12. Geophysical parameter estimations (amplitudes of the seasonal motion and elevations) of the area by PSI and RoMIO + PSI with 20 and 9 SAR images. Consistent with the simulations, the proposed method can achieve a more robust estimation result than the classical PSI. In particular, under a limited number of images, the interpretation of the parameters retrieved by PSI is severely influenced by outliers. The results of the proposed method are more interpretable. One can observe that the amplitudes of the motion tend to increase from one side to the other. One plausible reason is that the deformation allowances on the two sides of the bridge are different. To verify this, a very high-resolution image of the bridge is shown in Fig. 10 (middle). Interesting to note is that there are four elevated regions that correspond to the four lampposts on the bridge. We plot the corresponding two profiles from the results of PSI and RoMIO + PSI in Fig. 17.

processed the four parts of the whole InSAR phase stack as cropped with the red dashed rectangles shown in Fig. 13 (left). To its right, we also provide the associated optical image from Google Earth. Similar to the previous experiment, we estimate the geophysical parameters by PSI and by the proposed method with a substack (nine SAR images), which were selected according to the same baseline criteria described in the previous paragraph. In Fig. 14, the 2-D distribution of spatial and temporal baselines of the total 29 measurements is demonstrated, along with those of the selected nine measurements for reconstruction. The results are shown in Fig. 20. Besides, we manually added 50% outliers to the stack and demonstrated the parameters retrieved by PSI and RoMIO + PSI with 29 SAR images in Fig. 21.

V. Discussion

A. Performance in Simulations

According to the results shown in Fig. 7, although the NL-InSAR result can maintain the smooth fringes very well, the edges of the rectangle in the middle are more blurred compared with the other two results. This can be clearly observed in Fig. 8. Compared with HoRPCA, the proposed method can better keep the original structure of the interferogram, since it can better capture the low-rank structure of the data and model the sparse outliers by enhancing the low rank and the sparsity. Consistently, the evaluation in Table II shows that under 30% of outliers, both NL-InSAR and RoMIO can achieve reliable results. However, when the data are severely corrupted by outliers, e.g., 50% outliers, RoMIO can achieve a more robust performance than NL-InSAR.

Combining multipass InSAR techniques, e.g., PSI, with RoMIO can greatly improve the accuracy of parameter estimates. As shown in Fig. 9, the results of PSI contain outliers. This is especially true for the result from a subset of the stack. The reason is that the periodogram used PSI is only asymptotically optimal, which means large bias is very likely to occur at a low number of images. In contrast, the proposed method can robustly recover the parameters both using the full stack and using a subset of the stack.

Fig. 13. (Left) TerraSAR-X test image of the Las Vegas Convention Center. Since the building structure is complex and its spatial area is large (800 × 850 pixels), we separately process the four parts of the whole InSAR phase stack as cropped with the red dashed rectangles in the figure. (Right) Associated optical image from Google Earth.

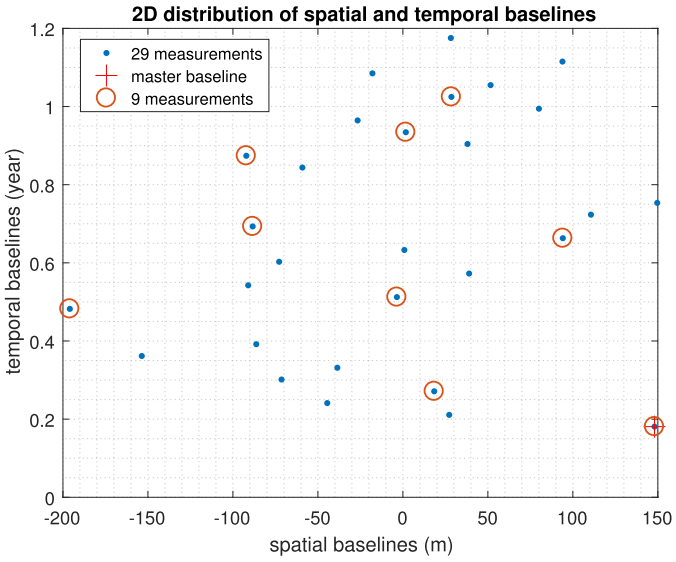

Fig. 14. 2-D distribution of spatial and temporal baselines of the total 29 measurements is demonstrated, along with those of the selected nine measurements for reconstruction. The baselines were also chosen to be close to uniform distribution.

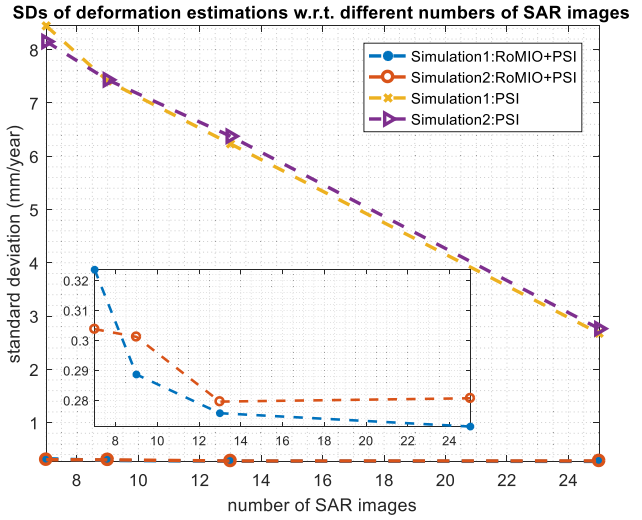

Fig. 15. SDs of deformation estimations with respect to different numbers of SAR images for reconstruction. The proposed method can achieve an SD around 0.3 [mm/year], which can improve the estimation accuracy of PSI more than ten times. It shows that the accuracy of RoMIO + PSI can be maintained at a better and more constant level compared with the PSI, whose efficiency decreases linearly with respect to the number of images. At the number of images down to 7, the accuracy of RoMIO + PSI still keeps at a submillimeter range, which is about 30 times better than PSI. This creates an opportunity of multipass InSAR geophysical parameter reconstruction using very small stacks.

That is to say the proposed method can, in turn, effectively reduce the number of images required for a reliable estimation. For the quantitative performance, as shown in Table III, we can see that the proposed geophysical parameter retrieval method—RoMIO + PSI—can improve the accuracy by a factor of 10–30 compared with PSI. This is also transferable to real data, as the simulation closely resembles real TerraSAR-X data. However, some artifacts are observed in the middle of the deformation estimates, which may be caused by choosing a large patch size (128 × 128) for optimization. Since the spatial information of phase tensors is utilized in the proposed approach, we found that with large patch sizes, oversmoothing

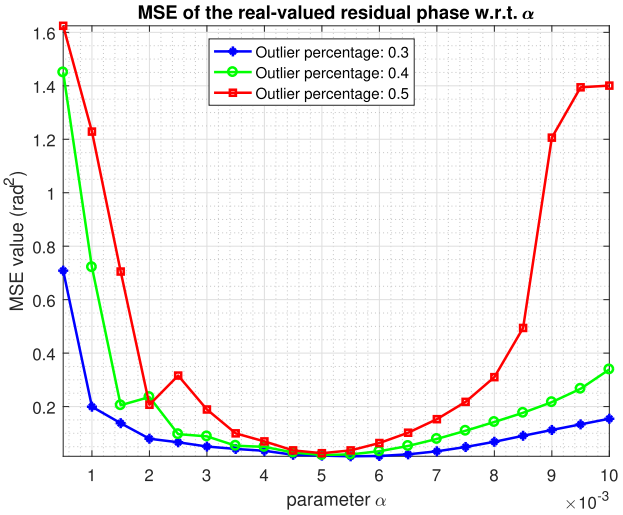

Fig. 16. MSE values of the real-valued residual phases between the phase tensor (Simulation 1) recovered by RoMIO and its ground truth with respect to different parameter (α) values. As shown in the figure, even under a high percentage of outliers, e.g., 30%, the operative range of α still keeps relatively wide. Of course, this range decreases as the percentage of outliers increases. Also, the parameter can also be tuned using the L-curve method [1], [60]. Still, for a particular data set, the optimal α for different percentages of outliers is similar (around 5×10^{-3} in our simulation), which means that no assumptions about the amount of outliers are required.

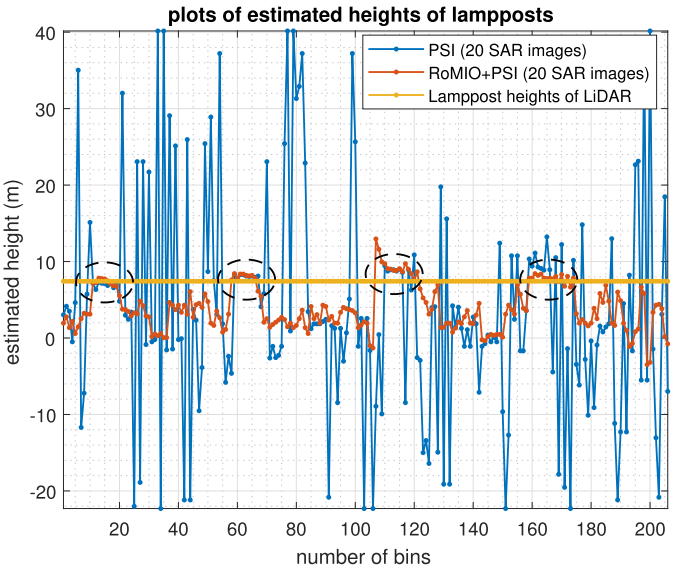

Fig. 17. Extracted two profiles of height estimates located at the yellow arrow positions of the results of PSI and RoMIO + PSI along with the lamppost height profile of LiDAR. Obviously, the four lampposts (shown by the black dashed ellipses) are well distinguishable in the result of the proposed method.

artifacts may exist, especially in geometrically complex areas.

As shown in Fig. 15, according to the results of the deformation reconstruction with decreasing numbers of SAR images, the proposed method can achieve an SD around 0.3 [mm/year], which can improve the estimation accuracy of PSI more than ten times.

Fig. 15 shows that the accuracy of RoMIO + PSI can be maintained at a better and more constant level compared with the PSI whose efficiency decreases linearly with respect to

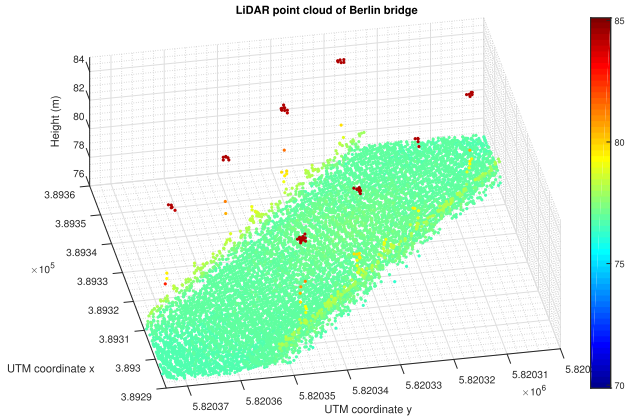

Fig. 18. LiDAR point cloud of the study Berlin bridge.

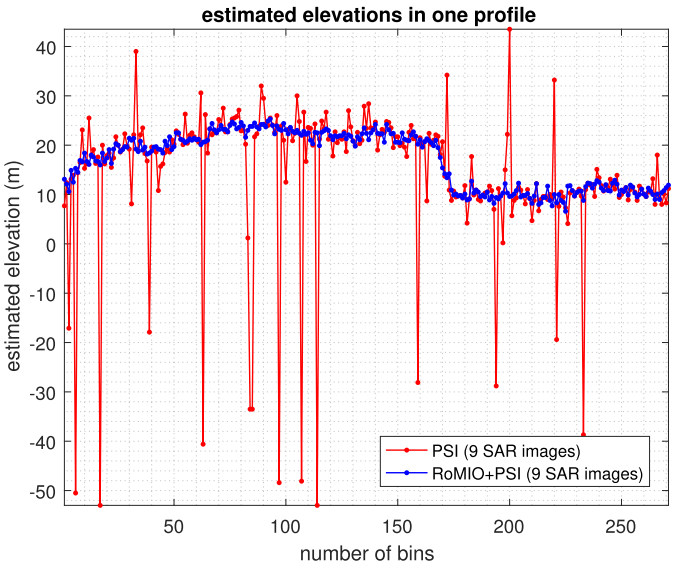

Fig. 19. Estimated elevation profiles of the two methods, which are selected by the yellow arrows in Fig. 20. The proposed method can preserve resolution by demonstrating a more obvious elevation step jumping than PSI and simultaneously mitigate incorrectly estimated points.

the number of images. At the number of images down to 7, the accuracy of RoMIO + PSI still keeps at a submillimeter range, which is about 30 times better than PSI. This creates an opportunity of multipass InSAR geophysical parameter reconstruction using very small stacks.

B. Parameter Selection

The two parameters of RoMIO are μ and γ, where μ comes with the introduced Lagrange multiplier term, and γ controls the balance between the low-rank tensor $\mathcal{X}$ and the outlier tensor $\mathcal{E}$. As introduced in [51], we can keep μ constant with the value $10 \times \text{std}(\text{vec}(\mathcal{G}))$. For tuning γ, we first rewrite γ as $\gamma = \alpha \times \lambda_*$, where a good choice for λ_* can be set as $(1/(\max(I_1, I_2, \ldots, I_N))^{1/2})$ according to [48] and [51], and α is a factor for tuning. To show the influence of α, Fig. 16 presents the MSE values of the real-valued residual phases of the phase stack recovered by RoMIO with respect to α (from 0.5×10^{-3} to 1×10^{-2}), under different

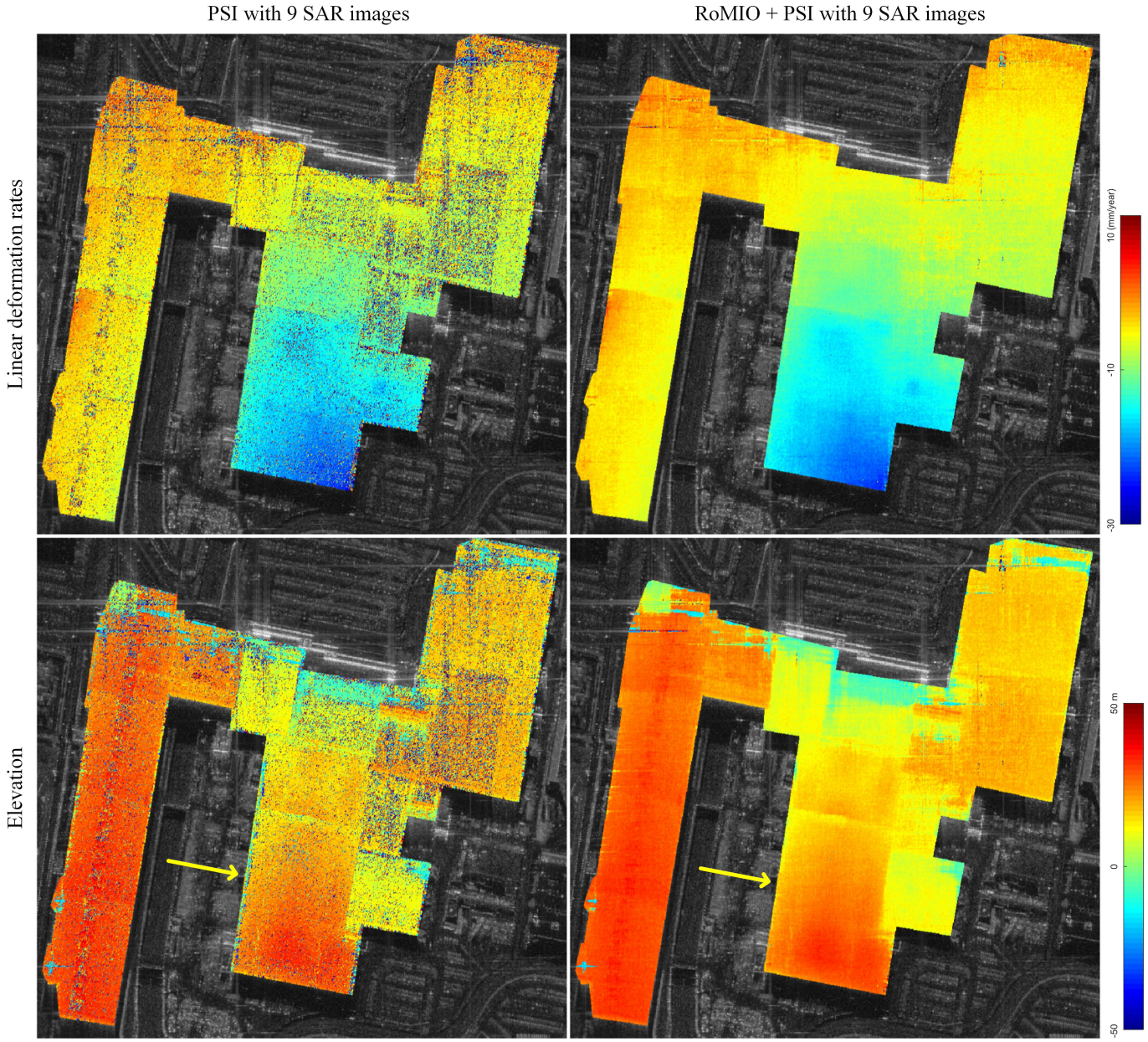

Fig. 20. Geophysical parameter estimations (linear deformation rates and elevations) of the Las Vegas Convention Center by PSI and RoMIO + PSI with nine SAR images (29 images in total). The proposed method can mitigate incorrectly estimated geophysical parameters much better than PSI. Meanwhile, it is worth noting that the geometric structures of the building can be preserved well.

percentages of outliers. As shown in the plot, even under a high percentage of outliers, e.g., 30%, the operable range of α still keeps relatively wide. Of course, this range decreases as the percentage of outliers increases. Still, the parameter can be tuned using the L-curve method [1], [60]. For a particular data set, the optimal α for different percentages of outliers is similar (around 5×10^{-3} in our simulation), which means that no assumptions about the amount of outliers are required.

C. Performance in Real Data

As shown in Fig. 12, consistent with the simulations, the proposed method can achieve a more robust estimation result than the classical PSI. In particular, in case of a limited number of images, the interpretation of the parameters retrieved by PSI is severely influenced by outliers. The results of the proposed method are more interpretable. One can observe that the amplitudes of the motion tend to increase from one side to the other. One plausible reason is that the deformation allowances on the two sides of the bridge are different. To verify this, a very high-resolution image of the bridge is shown in Fig. 10 (middle). The yellow ellipses in the image show that there exists certain mechanical clearance between the bridge body and the road it attaches to. Interesting to note is that in the elevation maps in Fig. 12, there are four elevated regions that correspond to the four lampposts

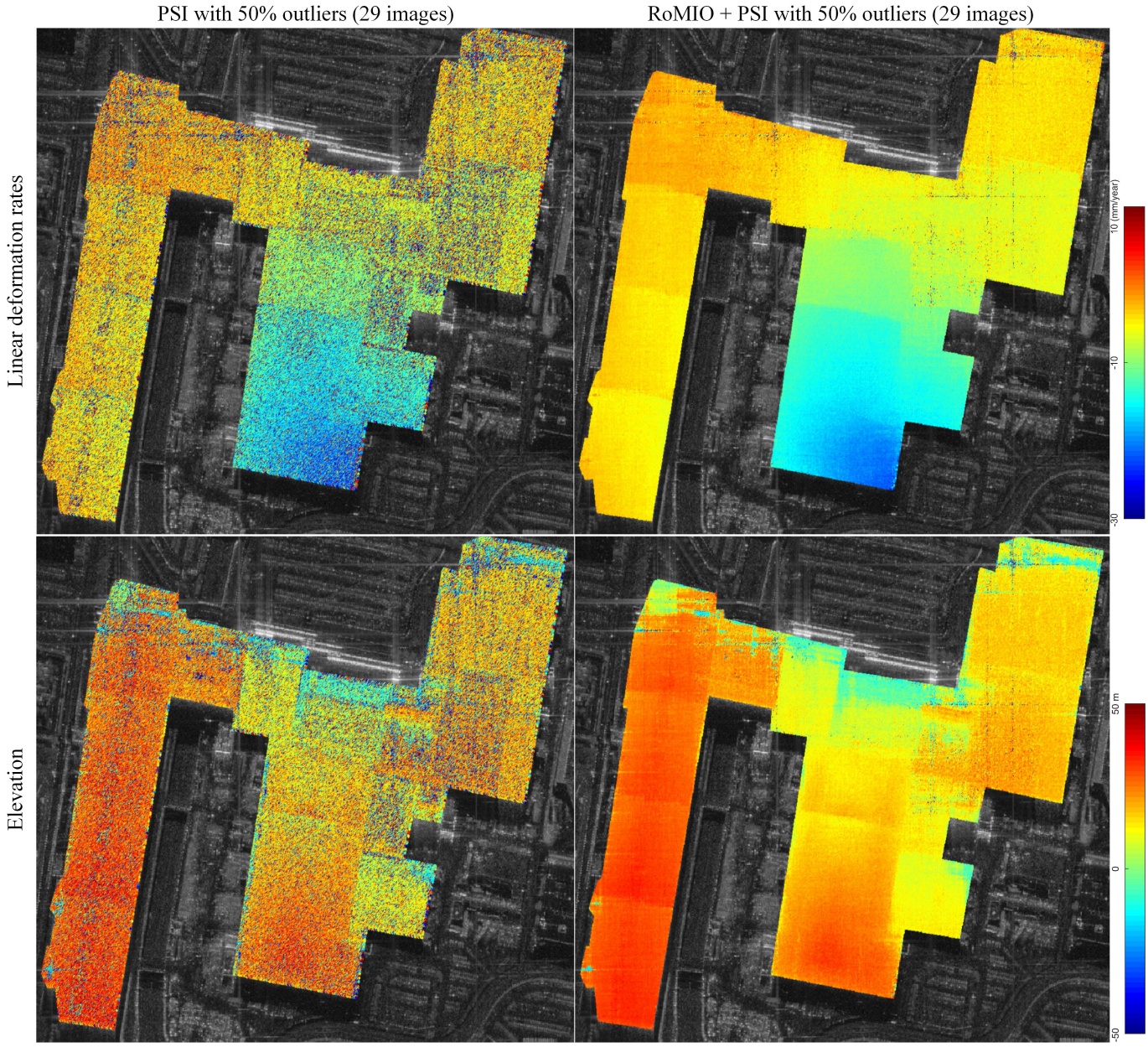

Fig. 21. Geophysical parameter estimations (linear deformation rates and elevations) of the Las Vegas Convention Center by PSI and RoMIO + PSI under the stack corrupted by 50% outliers. The geometric structures of the building cannot be well interpreted by the results of PSI. In contrast, our method can achieve much more reliable results than PSI.

on the bridge. We plot the corresponding profiles of height estimates from the results of PSI and RoMIO + PSI in Fig. 17. Obviously, the four lampposts are well distinguishable in the result of the proposed method. In order to quantitatively evaluate the performance of the proposed method, the result in Fig. 17 is compared with a centimeter-accuracy LiDAR point cloud shown in Fig. 18. As InSAR is relative measurement, we robustly adjust the height of bridge surface to match that in the LiDAR point cloud and then compare the height of lampposts to those in the LiDAR point cloud. To obtain the height of bridge surface as well as the height of lampposts in the two InSAR point clouds and the LiDAR point cloud, we *robustly average* the points within the yellow polygons shown in Fig. 12, respectively. According to the incidence angle ($\theta = 36.1°$), the estimated heights of the four lampposts based on the two methods are shown in Table IV. On the one hand, for such high SNR areas, PSI can achieve a reliable estimation result, while the proposed method indeed increases the height estimates with smaller bias and SD. On the other hand, as shown in Figs. 12 and 17, for those areas with low SNR such as bridge surface, the proposed method can also obtain much more robust estimates than PSI.

In the results of Las Vegas Convention Center shown in Fig. 20, the proposed method can mitigate the incorrectly estimated geophysical parameters much better than PSI, under limited SAR images. Besides, it is worth noting that the

TABLE IV
LAMPPOST HEIGHT ESTIMATIONS OF THE TWO METHODS WITH 20 SAR IMAGES, ALONG WITH THE REFERENCE OF LIDAR POINT CLOUD

Unit (m)	Lamppost1	Lamppost2	Lamppost3	Lamppost4
LiDAR height	7.42			
PSI mean	6.76	7.70	8.82	10.03
PSI SD	1.39	2.17	0.26	2.56
RoMIO+PSI mean	7.13	7.69	8.91	8.01
RoMIO+PSI SD	1.30	1.74	0.28	0.46

geometric structure of the object can be well preserved. For instance, as shown in Fig. 19, we plot the elevation profiles indicated by the yellow arrows from the two results in Fig. 20. The proposed method can preserve resolution by displaying a more obvious elevation step jumping than PSI and simultaneously mitigates outliers. Moreover, when we synthetically corrupt the data by 50% of outliers, the geometric structures of the building cannot be well interpreted by the results of PSI, as shown in Fig. 21. In contrast, the proposed method can achieve much more reliable results.

VI. CONCLUSION

This paper studied the low-rank property of object-based InSAR phase stacks and proposed RoMIO. RoMIO can be combined with conventional multipass InSAR techniques to improve the estimation accuracy of geophysical parameters. Taking PSI as an example, this paper demonstrated that in typical condition of very high-resolution spaceborne InSAR data, e.g., object size of 10 m, 5–dB SNR, and 10—20 SAR images, the proposed approach can improve the estimation accuracy of geophysical parameters by a factor of 10–30, especially in the presence of outliers. These merits can, in turn, efficiently reduce the number of SAR images for a reliable estimation.

Based on our experiments, we can see that the spatial sizes of tensors can influence the efficiency of the proposed method. On the one hand, with large spatial sizes, the low-rank property of the phase tensor is generally more prominent, which gives a wide operable range of the regularization parameters in the optimization. But oversmoothing artifacts may exist especially in some geometrically complex areas. On the other hand, with small spatial sizes, although it can be a benefit for preserving small detail, the regularization parameters must be carefully tuned. Otherwise, the reconstructed phase tensor may have the risk to be turned into a rank-1 tensor. Therefore, the tensor size should be large enough to promote low rankness of the true phase and the sparsity of outliers, but small enough to exclude complicated structures. According to the experiments in this paper, the typical patch size we utilized is around 100×100 pixels, and this can be improved by exploiting adaptive window.

Besides, the proposed approach is suitable for operational processing, as the only parameter that needs to be tuned, i.e., α, was shown to usually lie in the range from 1×10^{-3} to 1×10^{-1} based on both the simulated and real data experiments. Besides, the approach can easily be parallelized by carrying it out patchwisely.

Currently, this approach relies on the segmentation of objects. For future work, we would like to investigate lower level geometric information in SAR images to relax the requirement of object masks. Furthermore, we are also planning to research objects in nonurban areas, where a few of them present regular shapes, and attempt to investigate their inherent property, which can be utilized for the improvement of geophysical parameter retrieval based on the geometric information.

ACKNOWLEDGMENT

The authors would like to thank H. Hirschmüller of DLR Institute of Robotics and Mechatronics for providing the orthorectified optical image of Berlin.

They would also like to thank the reviewers for their valuable suggestions.

REFERENCES

[1] J. Kang, Y. Wang, M. Körner, and X. X. Zhu, "Robust object-based multipass InSAR deformation reconstruction," *IEEE Trans. Geosci. Remote Sens.*, vol. 55, no. 8, pp. 4239–4251, Aug. 2017.

[2] A. Ferretti, C. Prati, and F. Rocca, "Permanent scatterers in SAR interferometry," *IEEE Trans. Geosci. Remote Sens.*, vol. 39, no. 1, pp. 8–20, Jan. 2001.

[3] N. Adam, B. Kampes, M. Eineder, J. Worawattanamateekul, and M. Kircher, "The development of a scientific permanent scatterer system," in *Proc. ISPRS Workshop High Resolution Mapping Space*, Hannover, Germany, 2003, pp. 1–6.

[4] G. Fornaro, A. Pauciullo, and F. Serafino, "Deformation monitoring over large areas with multipass differential SAR interferometry: A new approach based on the use of spatial differences," *Int. J. Remote Sens.*, vol. 30, no. 6, pp. 1455–1478, 2009.

[5] J. J. Sousa, A. J. Hooper, R. F. Hanssen, L. C. Bastos, and A. M. Ruiz, "Persistent scatterer InSAR: A comparison of methodologies based on a model of temporal deformation vs. spatial correlation selection criteria," *Remote Sens. Environ.*, vol. 115, no. 10, pp. 2652–2663, 2011.

[6] S. Gernhardt and R. Bamler, "Deformation monitoring of single buildings using meter-resolution SAR data in PSI," *ISPRS J. Photogram. Remote Sens.*, vol. 73, pp. 68–79, Sep. 2012.

[7] B. M. Kampes, *Radar Interferometry*. Dordrecht, The Netherlands: Springer, 2006.

[8] Y. Wang, X. X. Zhu, and R. Bamler, "An efficient tomographic inversion approach for urban mapping using meter resolution SAR image stacks," *IEEE Geosci. Remote Sens. Lett.*, vol. 11, no. 7, pp. 1250–1254, Jul. 2014.

[9] M. Costantini, S. Falco, F. Malvarosa, F. Minati, F. Trillo, and F. Vecchioli, "Persistent scatterer pair interferometry: Approach and application to COSMO-SkyMed SAR data," *IEEE J. Sel. Topics Appl. Earth Observ. Remote Sens.*, vol. 7, no. 7, pp. 2869–2879, Jul. 2014.

[10] L. Zhang, X. Ding, and Z. Lu, "Modeling PSInSAR time series without phase unwrapping," *IEEE Trans. Geosci. Remote Sens.*, vol. 49, no. 1, pp. 547–556, Jan. 2011.

[11] A. De Maio, G. Fornaro, and A. Pauciullo, "Detection of single scatterers in multidimensional SAR imaging," *IEEE Trans. Geosci. Remote Sens.*, vol. 47, no. 7, pp. 2284–2297, Jul. 2009.

[12] A. Ferretti, A. Fumagalli, F. Novali, C. Prati, F. Rocca, and A. Rucci, "A new algorithm for processing interferometric data-stacks: SqueeSAR," *IEEE Trans. Geosci. Remote Sens.*, vol. 49, no. 9, pp. 3460–3470, Sep. 2011.

[13] K. Goel and N. Adam, "An advanced algorithm for deformation estimation in non-urban areas," *ISPRS J. Photogramm. Remote Sens.*, vol. 73, pp. 100–110, Sep. 2012.

[14] Y. Wang, X. X. Zhu, and R. Bamler, "Retrieval of phase history parameters from distributed scatterers in urban areas using very high resolution SAR data," *ISPRS J. Photogramm. Remote Sens.*, vol. 73, pp. 89–99, Sep. 2012.

[15] M. Jiang, X. Ding, R. F. Hanssen, R. Malhotra, and L. Chang, "Fast statistically homogeneous pixel selection for covariance matrix estimation for multitemporal InSAR," *IEEE Trans. Geosci. Remote Sens.*, vol. 53, no. 3, pp. 1213–1224, Mar. 2015.

[16] S. Samiei-Esfahany, J. E. Martins, F. van Leijen, and R. F. Hanssen, "Phase estimation for distributed scatterers in InSAR stacks using integer least squares estimation," *IEEE Trans. Geosci. Remote Sens.*, vol. 54, no. 10, pp. 5671–5687, Oct. 2016.

[17] Y. Wang and X. X. Zhu, "Robust estimators for multipass SAR interferometry," *IEEE Trans. Geosci. Remote Sens.*, vol. 54, no. 2, pp. 968–980, Feb. 2016.

[18] G. Fornaro, F. Serafino, and F. Soldovieri, "Three-dimensional focusing with multipass SAR data," *IEEE Trans. Geosci. Remote Sens.*, vol. 41, no. 3, pp. 507–517, Mar. 2003.

[19] F. Lombardini, "Differential tomography: A new framework for SAR interferometry," *IEEE Trans. Geosci. Remote Sens.*, vol. 43, no. 1, pp. 37–44, Jan. 2005.

[20] X. X. Zhu and R. Bamler, "Very high resolution spaceborne SAR tomography in urban environment," *IEEE Trans. Geosci. Remote Sens.*, vol. 48, no. 12, pp. 4296–4308, Dec. 2010.

[21] X. X. Zhu and R. Bamler, "Let's do the time warp: Multicomponent nonlinear motion estimation in differential SAR tomography," *IEEE Geosci. Remote Sens. Lett.*, vol. 8, no. 4, pp. 735–739, Jul. 2011.

[22] D. Reale, G. Fornaro, A. Pauciullo, X. Zhu, and R. Bamler, "Tomographic imaging and monitoring of buildings with very high resolution SAR data," *IEEE Geosci. Remote Sens. Lett.*, vol. 8, no. 4, pp. 661–665, Jul. 2011.

[23] G. Fornaro, F. Lombardini, A. Pauciullo, D. Reale, and F. Viviani, "Tomographic processing of interferometric SAR data: Developments, applications, and future research perspectives," *IEEE Signal Process. Mag.*, vol. 31, no. 4, pp. 41–50, Jul. 2014.

[24] X. X. Zhu and R. Bamler, "Tomographic SAR inversion by L_1 norm regularization—The compressive sensing approach," *IEEE Trans. Geosci. Remote Sens.*, vol. 48, no. 10, pp. 3839–3846, Oct. 2010.

[25] A. Budillon, A. Evangelista, and G. Schirinzi, "Three-dimensional SAR focusing from multipass signals using compressive sampling," *IEEE Trans. Geosci. Remote Sens.*, vol. 49, no. 1, pp. 488–499, Jan. 2011.

[26] X. X. Zhu and R. Bamler, "Superresolving SAR tomography for multidimensional imaging of urban areas: Compressive sensing-based TomoSAR inversion," *IEEE Signal Process. Mag.*, vol. 31, no. 4, pp. 51–58, Jul. 2014.

[27] M. Eineder, C. Minet, P. Steigenberger, X. Cong, and T. Fritz, "Imaging geodesy—Toward centimeter-level ranging accuracy with TerraSAR-X," *IEEE Trans. Geosci. Remote Sens.*, vol. 49, no. 2, pp. 661–671, Feb. 2011.

[28] C. Gisinger *et al.*, "Precise three-dimensional stereo localization of corner reflectors and persistent scatterers with TerraSAR-X," *IEEE Trans. Geosci. Remote Sens.*, vol. 53, no. 4, pp. 1782–1802, Apr. 2015.

[29] X. X. Zhu, S. Montazeri, C. Gisinger, R. F. Hanssen, and R. Bamler, "Geodetic SAR tomography," *IEEE Trans. Geosci. Remote Sens.*, vol. 54, no. 1, pp. 18–35, Jan. 2016.

[30] N. Cao, H. Lee, and H. C. Jung, "A phase-decomposition-based PSInSAR processing method," *IEEE Trans. Geosci. Remote Sens.*, vol. 54, no. 2, pp. 1074–1090, Feb. 2016.

[31] M. Schmitt, J. L. Schönberger, and U. Stilla, "Adaptive covariance matrix estimation for multi-baseline InSAR data stacks," *IEEE Trans. Geosci. Remote Sens.*, vol. 52, no. 11, pp. 6807–6817, Nov. 2014.

[32] M. Schmitt and U. Stilla, "Adaptive multilooking of airborne single-pass multi-baseline InSAR stacks," *IEEE Trans. Geosci. Remote Sens.*, vol. 52, no. 1, pp. 305–312, Jan. 2014.

[33] G. Fornaro, S. Verde, D. Reale, and A. Pauciullo, "CAESAR: An approach based on covariance matrix decomposition to improve multibaseline–multitemporal interferometric SAR processing," *IEEE Trans. Geosci. Remote Sens.*, vol. 53, no. 4, pp. 2050–2065, Apr. 2015.

[34] M. Neumann, L. Ferro-Famil, and A. Reigber, "Estimation of forest structure, ground, and canopy layer characteristics from multibaseline polarimetric interferometric SAR data," *IEEE Trans. Geosci. Remote Sens.*, vol. 48, no. 3, pp. 1086–1104, Mar. 2010.

[35] S. Tebaldini, "Single and multipolarimetric SAR tomography of forested areas: A parametric approach," *IEEE Trans. Geosci. Remote Sens.*, vol. 48, no. 5, pp. 2375–2387, May 2010.

[36] M. Schmitt and U. Stilla, "Maximum-likelihood-based approach for single-pass synthetic aperture radar tomography over urban areas," *IET Radar, Sonar Navigat.*, vol. 8, no. 9, pp. 1145–1153, 2014.

[37] C.-A. Deledalle, L. Denis, and F. Tupin, "NL-InSAR: Nonlocal interferogram estimation," *IEEE Trans. Geosci. Remote Sens.*, vol. 49, no. 4, pp. 1441–1452, Apr. 2011.

[38] X. X. Zhu, R. Bamler, M. Lachaise, F. Adam, Y. Shi, and M. Eineder, "Improving TanDEM-X DEMs by non-local InSAR filtering," in *Proc. EUSAR 10th Eur. Conf. Synth. Aperture Radar*, 2014, pp. 1–4.

[39] C.-A. Deledalle, L. Denis, G. Poggi, F. Tupin, and L. Verdoliva, "Exploiting patch similarity for SAR image processing: The nonlocal paradigm," *IEEE Signal Process. Mag.*, vol. 31, no. 4, pp. 69–78, Jul. 2014.

[40] F. Sica, D. Reale, G. Poggi, L. Verdoliva, and G. Fornaro, "Nonlocal adaptive multilooking in SAR multipass differential interferometry," *IEEE J. Sel. Topics Appl. Earth Observ. Remote Sens.*, vol. 8, no. 4, pp. 1727–1742, Apr. 2015.

[41] X. X. Zhu, N. Ge, and M. Shahzad, "Joint sparsity in SAR tomography for urban mapping," *IEEE J. Sel. Topics Signal Process.*, vol. 9, no. 8, pp. 1498–1509, Dec. 2015.

[42] J. Kang, Y. Wang, M. Körner, and X. X. Zhu, "Object-based InSAR deformation reconstruction with application to bridge monitoring," in *Proc. IEEE Int. Geosci. Remote Sens. Symp. (IGARSS)*, Jun. 2016, pp. 6871–6874.

[43] X. Zhou, C. Yang, H. Zhao, and W. Yu, "Low-rank modeling and its applications in image analysis," *ACM Comput. Surv.*, vol. 47, no. 2, p. 36, 2015.

[44] I. T. Jolliffe, *Principal Component Analysis*. Hoboken, NJ, USA: Wiley, 2002.

[45] O. Yousif and Y. Ban, "Improving urban change detection from multitemporal SAR images using PCA-NLM," *IEEE Trans. Geosci. Remote Sens.*, vol. 51, no. 4, pp. 2032–2041, Apr. 2013.

[46] G. Chen and S.-E. Qian, "Denoising of hyperspectral imagery using principal component analysis and wavelet shrinkage," *IEEE Trans. Geosci. Remote Sens.*, vol. 49, no. 3, pp. 973–980, Mar. 2011.

[47] H. Yao and L. Tian, "A genetic-algorithm-based selective principal component analysis (GA-SPCA) method for high-dimensional data feature extraction," *IEEE Trans. Geosci. Remote Sens.*, vol. 41, no. 6, pp. 1469–1478, Jun. 2003.

[48] E. J. Candès, X. Li, Y. Ma, and J. Wright, "Robust principal component analysis?" *J. ACM*, vol. 58, no. 3, p. 11, May 2011.

[49] H. Zhang, W. He, L. Zhang, H. Shen, and Q. Yuan, "Hyperspectral image restoration using low-rank matrix recovery," *IEEE Trans. Geosci. Remote Sens.*, vol. 52, no. 8, pp. 4729–4743, Aug. 2014.

[50] L. Borcea, T. Callaghan, and G. Papanicolaou, "Synthetic aperture radar imaging and motion estimation via robust principal component analysis," *SIAM J. Imag. Sci.*, vol. 6, no. 3, pp. 1445–1476, 2013.

[51] D. Goldfarb and Z. Qin, "Robust low-rank tensor recovery: Models and algorithms," *SIAM J. Matrix Anal. Appl.*, vol. 35, no. 1, pp. 225–253, 2014.

[52] T. G. Kolda and B. W. Bader, "Tensor decompositions and applications," *SIAM Rev.*, vol. 51, no. 3, pp. 455–500, 2009.

[53] A. Cichocki *et al.*, "Tensor decompositions for signal processing applications: From two-way to multiway component analysis," *IEEE Signal Process. Mag.*, vol. 32, no. 2, pp. 145–163, Mar. 2015.

[54] L. De Lathauwer, B. De Moor, and J. Vandewalle, "Singular value decomposition," in *Proc. EUSIPCO*, vol. 1. Edinburgh, Scotland, U.K., 1994, pp. 175–178.

[55] L. De Lathauwer, B. De Moor, and J. Vandewalle, "A multilinear singular value decomposition," *SIAM J. Matrix Anal. Appl.*, vol. 21, no. 4, pp. 1253–1278, 2000.

[56] E. J. Candès, M. B. Wakin, and S. P. Boyd, "Enhancing sparsity by reweighted ℓ_1 minimization," *J. Fourier Anal. Appl.*, vol. 14, nos. 5–6, pp. 877–905, 2008.

[57] Y. G. Peng, J. L. Suo, Q. H. Dai, and W. L. Xu, "Reweighted low-rank matrix recovery and its application in image restoration," *IEEE Trans. Cybern.*, vol. 44, no. 12, pp. 2418–2430, Dec. 2014.

[58] S. Boyd, N. Parikh, E. Chu, B. Peleato, and J. Eckstein, "Distributed optimization and statistical learning via the alternating direction method of multipliers," *Found. Trends Mach. Learn.*, vol. 3, no. 1, pp. 1–122, Jan. 2011.

[59] S. Gu, L. Zhang, W. Zuo, and X. Feng, "Weighted nuclear norm minimization with application to image denoising," in *Proc. IEEE Conf. Comput. Vis. Pattern Recognit.*, Jun. 2014, pp. 2862–2869.

[60] P. C. Hansen and D. P. O'Leary, "The use of the L-curve in the regularization of discrete ill-posed problems," *SIAM J. Sci. Comput.*, vol. 14, no. 6, pp. 1487–1503, 1993.

[61] H. Hirschmuller, "Stereo processing by semiglobal matching and mutual information," *IEEE Trans. Pattern Anal. Mach. Intell.*, vol. 30, no. 2, pp. 328–341, Feb. 2008.

Jian Kang (S'16) received the B.S. and M.E. degrees in electronic engineering from the Harbin Institute of Technology, Harbin, China, in 2013 and 2015, respectively. He is currently pursuing the Ph.D. degree with the Chair of Signal Processing in Earth Observation, Technical University of Munich, Munich, Germany.

His research interests include multidimensional data analysis, geophysical parameter estimation based on InSAR data, and machine learning in optical images.

Yuanyuan Wang (S'10–M'14) received the B.Eng. degree (Hons.) in electrical engineering from The Hong Kong Polytechnic University, Hong Kong, in 2008, and the M.Sc. and Dr.-Ing. degrees from the Technical University of Munich (TUM), Munich, Germany, in 2010 and 2015, respectively.

In 2014, he was a Guest Scientist with the Institute of Visual Computing, ETH Zürich, Zürich, Switzerland. He is currently with the Signal Processing in Earth Observation, TUM. His research interests include optimal and robust parameters estimation in multibaseline InSAR techniques, multisensor fusion algorithms of SAR and optical data, nonlinear optimization with complex numbers, and the applications of these techniques in urban and volcanic areas.

Dr. Wang was one of the best reviewers of the IEEE TRANSACTIONS ON GEOSCIENCE AND REMOTE SENSING 2016.

Michael Schmitt (S'08–M'14–SM'16) received the Dipl.-Ing. degree in geodesy and geoinformation and the Dr.-Ing. degree in remote sensing from the Technical University of Munich (TUM), Munich, Germany, in 2009 and 2014, respectively.

Since 2015, he has been a Senior Researcher and the Deputy Head at the Professorship for Signal Processing in Earth Observation, TUM. In 2016, he was a Guest Scientist with the University of Massachusetts Amherst, Amherst, MA, USA. His research interests include signal and image processing for the extraction of information from remote sensing data, sensor data fusion with emphasis on the joint exploitation of optical and radar data, 3-D reconstruction by techniques, such as SAR interferometry, SAR tomography, radargrammetry, or photogrammetry, and millimeter-wave SAR remote sensing.

Dr. Schmitt is a Co-Chair of the International Society for Photogrammetry and Remote Sensing Working Group I/3 on SAR and Microwave Sensing. He frequently serves as a reviewer for a number of renowned international journals. In 2013 and 2015, he was elected as the IEEE GEOSCIENCE AND REMOTE SENSING LETTERS Best Reviewer, leading to his appointment as an associate editor of the journal in 2016.

Xiao Xiang Zhu (S'10–M'12–SM'14) received the M.Sc. and Dr.-Ing. degrees and the Habilitation degree in signal processing from the Technical University of Munich (TUM), Munich, Germany, in 2008, 2011, and 2013, respectively.

She was a Guest Scientist or a Visiting Professor with the Italian National Research Council, Naples, Italy, in 2009, Fudan University, Shanghai, China, in 2014, The University of Tokyo, Tokyo, Japan, in 2015, and the University of California at Los Angeles, Los Angeles, CA, USA, in 2016. She is currently a Professor with Signal Processing in Earth Observation (SiPEO), TUM and the German Aerospace Center (DLR), Wessling, Germany, the Head of the Team—Signal Analysis, DLR, and the Head of the Helmholtz Young Investigator Group—SiPEO, DLR and TUM. Her research interests include remote sensing and earth observation, signal processing, machine learning, and data science, with a special application focus on global urban mapping.

Dr. Zhu is a member of the Young Academy (Junge Akademie/Junges Kolleg) at the Berlin-Brandenburg Academy of Sciences and Humanities and the German National Academy of Sciences Leopoldina, and the Bavarian Academy of Sciences and Humanities. She is an Associate Editor of the IEEE TRANSACTIONS ON GEOSCIENCE AND REMOTE SENSING.